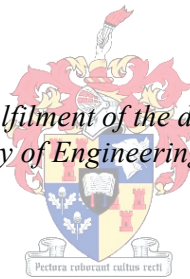


An Investigation into the Research and Development of Nanostructured Photovoltaic Cells

by
Alwyn Francois Botha

*Thesis presented in partial fulfilment of the degree of Master of Science in
Engineering at the Faculty of Engineering, Stellenbosch University*



Supervisor: Prof. Willem Jacobus Perold
Department of Electrical and Electronic Engineering

March 2010

Declaration

By submitting this thesis electronically, I declare that the entirety of the work contained therein is my own, original work, that I am the owner of the copyright thereof (unless to the extent explicitly otherwise stated) and that I have not previously in its entirety or in part submitted it for obtaining any qualification.

March 2010

Copyright © 2010 Stellenbosch University

All rights reserved

Abstract

An Investigation into the Research and Development of Nanostructured Photovoltaic Cells

A.F. Botha

Supervisor: Prof. Willem Jacobus Perold

Department of Electrical and Electronic Engineering

Thesis: MScEng (Electronic Engineering)

March 2010

Organic semiconductors are used to manufacture thin film (smaller than 50 nm) photovoltaic devices. Layer thicknesses are calibrated with the use of an AFM and QCM crystals. An in house method is prepared for solar cell comparison, and AM1.5G (one sun equivalent) testing is performed on manufactured solar cells. The importance of layer thickness and the exciton blocking layers are also highlighted.

Numerical modelling of the optical electric field amplitude is done by the transfer matrix method, to take optical interference effects into consideration. The photo generated current was extracted as a function of absorption with varying position in the active layers, and used to excite a general model for organic photovoltaic cells.

Uittreksel

'n Ondersoek na die navorsing en ontwikkeling van nano-gestruktureerde fotovoltaise selle

("Nanostructured Photovoltaic Cells: An Investigation into Research & Development")

A.F. Botha

Supervisor: Prof. Willem Jacobus Perold

Department of Electrical and Electronic Engineering

Tesis: MScIng (Elektroniese Ingenieurswese)

Maart 2010

Organiese halfgeleiers word gebruik vir die vervaardiging van dun-film (kleiner as 50 nm) fotovoltaise toestelle. Laagdiktes is gekalibreer deur die gebruik van 'n AFM en QCM kristalle. 'n Inhuis metode is voorberei vir die vergelyking van vervaardigde selle. Daarna is AM1.5G (een son ekwivalente) toetse uitgevoer op die vervaardigde sonselle. Die belangrikheid van laag dikte en die "exciton" blok lae word ook beklemtoon.

Numeriese modellering van die optiese elektriese veld amplitude word gedoen deur die oordrag matriks metode, om optiese interferensie gevolge in ag te neem. Die foto-gegenereerde stroom is as 'n funksie van absorpsie onttrek met wisselende posisie in die aktiewe lae, en is gebruik in 'n algemene model vir organiese fotovoltaise selle.

Acknowledgements

I would like to express my sincere gratitude to the following people and organisations without whom this research would not have been possible.

- The financial assistance of the South African National Energy Research Institute towards this research is hereby acknowledged. Opinions expressed and conclusions arrived at, are those of the author and are not necessarily to be attributed to SANERI.
- My supervisor Prof. W.J. Perold, for his continued support and encouragement.
- A special thanks to Ulrich Büttner, for his technical insight and guidance.
- Batsirai Magunje and The Department of Physics at the University of Cape Town, for use of their facilities and assistance in solar cell testing.
- Eric Tong Hoke and his advisor Professor Michael D. McGehee from Stanford University for their assistance in solving the Transfer Matrix Method in my simulations.
- Jeanette Cilliers and the Department of Microbiology for the long term loan of a pipette.
- All my friends and family for their continued support and time, especially in proof reading.

Dedications

To my parents, for all their hard work, providing me the opportunity to be in this position, and for all their motivation.

Contents

Declaration	i
Abstract	ii
Uittreksel	iii
Acknowledgements	iv
Dedications	v
Contents	vi
List of Figures	viii
List of Tables	xi
Nomenclature & Abbreviations	xii
1 Introduction	1
1.1 Motivation	1
1.2 Research Objectives	1
1.3 Thesis Outline	2
2 The Photoelectric Effect	3
2.1 Quantum Mechanics of the Sun	3
2.2 The Photon	3
2.3 Photovoltaic Cells	4
2.4 Organic Solar Cells	5
2.5 Conclusion	8
3 Design	9
3.1 Configurations of Organic solar cells	9

3.2	Bi-layer or Heterojunction	12
3.3	Conclusion	16
4	The Manufacture of TFOSC	17
4.1	Equipment & Techniques	17
4.2	The first Design of an Heterojunction cell	20
4.3	Pyramid Heterojunction	25
4.4	Adding Exciton Blocking layers	26
4.5	Gold Sputtering	36
4.6	CuPc nanowires	37
4.7	Conclusion	38
5	Testing	39
5.1	Making Contact	39
5.2	AM1.5G	42
5.3	Conclusion	56
6	Simulation	58
6.1	Commercial Software	58
6.2	Equivalent Circuit Model	59
6.3	Optical Interference Method	60
6.4	IV Curves	70
6.5	Conclusion	74
7	Conclusion	75
7.1	Future Recommendations	75
	Appendices	78
A	Shadow Masks Used in Thermal Evaporation	79
B	Complex indices of refraction	83
C	TMM	86
	References	93

List of Figures

2.1	P/N junction indication direction of photocurrent [1].	4
3.1	Nanostructured solar cell.	11
3.2	First device layout.	12
3.3	Pyramid shaped solar cell.	13
3.4	Solar cell with BCP.	13
3.5	Solar cell with PEDOT:PSS added.	14
3.6	Energy diagram.	15
3.7	SEM images of CuPc layers deposited on Au substrates at various temperatures [2].	16
4.1	Thermal Evaporator situated in the cleanroom.	18
4.2	Photolithography Exposure.	19
4.3	Atomic Force Microscope as set up in the cleanroom.	20
4.4	AFM micro structure.	20
	(a) Topography Scan	20
	(b) 3-Dimensional View	20
4.5	Photoresist blocks on a polished MgO sample.	21
4.6	CuPc left on MgO after liftoff in acetone.	22
4.7	AFM tip placement	23
4.8	A 3-dimensional view of a scan.	24
4.9	Cross section of the step edge	24
4.10	Leftover BCP after liftoff in diluted photoresist remover.	27
4.11	BCP film as seen under an optical microscope when using rubylith to create a step edge.	28
4.12	The improvement in the BCP step edge from heating the Rubylith as seen under an optical microscope.	29
4.13	AFM tip positioning over a cross on ITO glass.	31
4.14	Surface roughness of ITO on glass.	31
4.15	Surface roughness of ITO on glass after adding PEDOT:PSS.	32

4.16	Surface roughness of ITO on glass after adding PEDOT:PSS zoomed in on a smaller area.	33
4.17	Topography scan of the cut made in the PEDOT layer with a surgical blade.	33
4.18	Cross section of a cut made in PEDOT to measure the depth.	34
4.19	Lithography setup.	35
4.20	A 3-dimensional view of the line the AFM scratched into the PEDOT layer.	35
4.21	A cross section through the scan, showing how the depth of the line scratched into the PEDOT was measured.	36
5.1	The deformation in the layers of the solar cell, made by placing the sample on wet conductive paint.	40
5.2	The deformation in the layers caused by acetone used to thin the conductive paint.	40
5.3	Cracks shown under optical microscope caused by the conductive paint crimping between the sample and PCB when it dries.	41
5.4	The glue on the copper tape deforming the layers. The damage looks like a tear in the films (a) and like crinkled layers under a optical microscope (b).	41
	(a) Tear	41
	(b) Tear under microscope	41
5.5	Screw connectors over the silver strips clamping the solar cell onto a PCB.	42
5.6	Zenith angle for Air Mass 1.5.	43
5.7	Lightbox used for solar cell testing.	44
5.8	IV curve for devices with a 15/35 and 15/45 semiconductor layer structures.	46
5.9	IV curve for a device with a 20/40 semiconductor layer structure.	47
5.10	IV curve for devices with a 15/40 and 10/40 semiconductor layer structures.	49
5.11	IV curves of all the variations in semiconductor thickness.	50
5.12	Completed solar cell as seen from the back.	51
5.13	Micron sized cracks in solar cell.	52
5.14	IV curve of two complete cells, including PEDOT, before and after QCM recalibration.	53
5.15	IV curves showing the variation in cells under AM1.5G	54
5.16	IV curve of repeated testing on the same cell	55

5.17	IV curve of cells with and without the BCP layer	56
5.18	Absorption of CuPc at various wavelengths.	57
6.1	Equivalent circuit model for photovoltaic cells	59
	(a) Ideal model for a solar cell	59
	(b) Real model for a solar cell	59
6.2	Equivalent circuit model as proposed by [3].	60
6.3	Equivalent circuit model as proposed by [4], used in this work.	60
6.4	Geometry of the semi-infinite layer stack used to model light propagation.	61
6.5	Simulated normalised plots of the optical electric field propagation. . .	64
6.6	Simulated normalised plots of the optical electric field at different indicated wavelengths.	64
6.7	Simulated Optical Electric Field propagation, illustrating the effect of varying PEDOT thickness.	65
	(a) PEDOT = 30 nm	65
	(b) PEDOT = 60 nm	65
6.8	Simulated Exciton Generation Rate, as a function of wavelength and position through the whole device, for several wavelengths.	67
	(a) λ at 300 nm and 400 nm	67
	(b) λ at 500 nm and 600 nm	67
	(c) λ at 700 nm and 800 nm	67
	(d) λ summed from 300 nm through to 900 nm	67
6.9	Short circuit photo current at different wavelengths, for different D/A interface thicknesses.	69
6.10	Simulated IV curve, with different cell area values.	71
6.11	Simulated IV curve, with different series resistance values.	72
6.12	Simulated IV curve, with different shunt resistance values.	72
6.13	Comparison between simulated and measured IV curve.	73
6.14	Comparison between simulated (corrected) and measured IV curve. . .	73
A.1	Mask assembly	80
A.2	Shadow mask for silver	80
A.3	Shadow mask for CuPc	81
A.4	Shadow mask for C ₆₀	81
A.5	Shadow mask for Aluminium	82
A.6	Shadow mask for BCP	82

List of Tables

2.1	Organic materials that can be used as electron donor/acceptor semiconductors [5].	6
4.1	Shadow masks used to create a pyramid structured solar cell through thermal evaporation.	25
4.2	Shadow masks used to create a pyramid structured solar cell through thermal evaporation, listed in order used.	29
4.3	Different surface roughness results for CuPc films, deposited at different temperatures on gold covered ITO glass.	37
5.1	Different layer thicknesses of organic semiconductors and results obtained.	46
5.2	Different layer thicknesses of organic semiconductors, with BCP, and results obtained.	48
5.3	Summary of experimental results under AM1.5 conditions.	57
B.1	Complex indices of refraction for PEDOT:PSS at different wavelengths taken from [6]	83
B.2	Complex indices of refraction for aluminium at different wavelengths taken from [7]	83
B.3	Complex indices of refraction for ITO at different wavelengths taken from [8]	84
B.4	Complex indices of refraction for BCP at different wavelengths taken from [9]	84
B.5	Complex indices of refraction for CuPc at different wavelengths taken from [10]	84
B.6	Complex indices of refraction for PEDOT:PSS at different wavelengths taken from [10]	85

Nomenclature & Abbreviations

Constants

$$\pi = 3.141\,592\,654$$

$$e = 2.718\,281\,828$$

$$h = 6.626068^{-34} \text{ Planck's constant}$$

$$c = 299792458 \text{ Speed of light} \dots\dots\dots [\text{m/s}]$$

Variables

$$d \quad \text{Thickness Coordinate} \dots\dots\dots [\text{m}]$$

$$G \quad \text{Exciton Generation rate Coordinate} \dots\dots\dots [\text{unitless}]$$

$$I \quad \text{Current Coordinate} \dots\dots\dots [\text{Ampere}]$$

$$L \quad \text{Length Coordinate} \dots\dots\dots [\text{m}]$$

$$V \quad \text{Voltage Coordinate} \dots\dots\dots [\text{Volt}]$$

$$x \quad \text{Coordinate} \dots\dots\dots [\text{m}]$$

$$\lambda \quad \text{Wavelength} \dots\dots\dots [\text{m}]$$

$$\theta \quad \text{Quantum Efficiency of Free Charge Generation} \dots\dots\dots [\text{unitless}]$$

$$\tau \quad \text{Exciton Lifetime} \dots\dots\dots [\text{s}]$$

Vectors

$$\bar{n} \quad \text{Complex index of refraction}$$

Matrices

$$I \quad \text{Interface Matrix}$$

L	Layer Matrix
S	Transfer Matrix

Subscripts

0	Initial/substrate
A	Absorption
CC	Charge Collection
D	Exciton Dissociation / Diffusion
ED	Exciton Diffusion
j	Layer

Superscripts

+	Positive x direction
-	Negative x direction

Abbreviations

A	Electron Acceptor
AFM	Atomic Force Microscope
AM	Air Mass
BCP	Bathocuprione
CB	Conduction Band
CuPc	Copper(II)Phthalocyanine
CVD	Chemical Vapour Deposition
D	Electron Donor
EA	Electron Affinity
EBL	Exciton Blocking Layer / Electron Beam Lithography
ENM	Engineering Nano Materials
EUVL	Extreme Ultra Violet Lithography

EQE	External Quantum Efficiency
FF	Fill Factor
FTO	Fluorine doped Tin Oxide
HOMO	Highest Occupied Molecular Orbital
ITO	Indium doped Tin Oxide
LiF	Lithium Fluoride
LUMO	Lowest Occupied Molecular Orbital
MIM	Metal- Insulator- Metal
PEDOT	Poly(3,4-ethylenedioxythiophene)
PEDOT:PSS	Poly(3,4-ethylenedioxythiophene) Poly(styrene sulfonate)
PV	Photovoltaic
QCM	Quartz Crystal Monitor
RPM	Revolution per Minute
TMM	Transfer Matrix Method
TFOSC	Thin Film Organic Solar Cells
UCT	University of Cape Town
UV	Ultraviolet
VB	Valence Band

Chapter 1

Introduction

1.1 Motivation

This thesis addresses two main avenues of research. Firstly nanotechnology: Nanotechnology is one of the fastest growing research fields worldwide, and studies are being conducted in various areas such as biomedical, drug delivery, automotive and energy. The last field, energy, is the second foundation for the motivation of this project. South Africa is still a country where energy is a commodity that not all people have access to. Photovoltaic cells could be one of many sustainable solutions to the growing energy shortage. Upon the completion of the aims of the thesis, this project could open doors for new research in every facet of the work done, not only efficiencies of solar cells, but also:

- research into more cost effective materials for solar cells
- thickness and layout of solar cells
- the construction of flexible cells, and possible applications thereof
- simpler manufacturing techniques
- studies on the lifetime of devices and the cumulative impact on the environment

1.2 Research Objectives

The objective of this thesis is not to create a new or more efficient type of solar cell. Rather the aim is to show the steps taken to construct a working solar cell,

albeit a small device in a laboratory, outlining all the difficulties encountered and the techniques used to work with the materials that make up such a solar cell. It aims then to be a platform to be used as reference for designing better ways of making solar energy cheaper, safer and easier to convert. As this project is part of the SAND (Superconductivity Advanced Materials, NANO Materials & Devices) group at Stellenbosch University, the solar cells researched will be thin film and/or nanostructured. This project aims to design and build a working thin film solar cell, to test the device and create a model to simulate and predict the behaviour of such a cell.

1.3 Thesis Outline

Chapter One serves as an introduction.

Chapter Two serves as a literature study and gives an overview of general photovoltaic cells, and deeper insight into the working of organic photovoltaic materials.

Chapter Three is dedicated to the design of a working solar cell. The designs are continually adapted in this chapter, to form a working device, and improve on its performance.

Chapter Four describes the methods used to manufacture the solar cells. This includes procedures used on the equipment available, material calibration and solutions to challenges faced to create the designs in Chapter 3.

Chapter Five shows how the devices designed in Chapter 3, and put together as described in Chapter 4, are tested. This includes building a cost effective in-house method of comparing devices to one another, as well as 1-sun equivalent testing.

Chapter Six implements a model to predict the behaviour of organic photovoltaic devices, as well as using the TMM to try and predict the photo generated current.

Chapter Seven summarises the results obtained and makes some suggestions for future improvements.

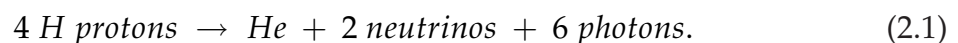
Chapter 2

The Photoelectric Effect

This chapter documents the literature study done on solar cells. It describes the behaviour of different solar cells and ends with a description of organic photovoltaic cells, the focus of this thesis.

2.1 Quantum Mechanics of the Sun

It comes as no surprise that the sun has received a lot of interest for its use as an energy supply. Consisting of 99.86% of the mass in our solar system, the sun, mostly hydrogen plasma, creates its energy through nuclear fusion with a core temperature of 16×10^6 Kelvin. Simply put, inside the sun four single nucleus hydrogen atoms are forced together to form a new nucleus consisting of two protons and two neutrons, called helium. The mass of the nucleus of the newly fused helium atom is less than the mass of the four hydrogen atoms added together. According to Einstein's relation $E = mc^2$, the leftover mass is converted to 25 MeV of energy consisting of two neutrinos and six photons [11],



2.2 The Photon

Remarkably, photons can travel from the sun to the earth's surface where it can be harvested to create electricity in only 8 minutes [11]. The energy in a photon is calculated from

$$E = \frac{h \cdot c}{\lambda}, \quad (2.2)$$

where h is Planck's constant, c is the speed of light and λ is the wavelength of light [12]. Photons with energy exceeding the bandgap of the material it is entering, can be absorbed to create an electron-hole pair.

2.3 Photovoltaic Cells

Photovoltaic cells, also referred to as solar cells, are devices that convert light into electricity. To achieve this, a device absorbs the photons in the light and uses them to form charge carriers. How these devices achieve this, differ slightly in different types of solar cells. A couple of different devices are discussed in the following sections.

Among the inorganic materials, silicon has for a long time been the material used in commercially available solar cells. Silicon can be doped to be a n-type semiconductor with group V elements such as phosphorous, or p-type, with group 3 elements such as boron. Both these states are commercially available, and can then be doped from one side to form a p/n junction. When a p/n junction is formed, as shown in Figure 2.1, an internal electric field is formed. It is in this E-field where photons are absorbed and free holes and electrons are created. The charge difference in the E-field and surrounding p/n junction is then able to drive current flow by extracting the holes and electrons when a load is connected.

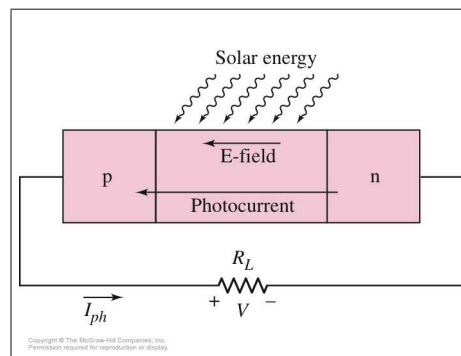


Figure 2.1: P/N junction indication direction of photocurrent [1].

However, direct bandgap materials such as gallium arsenide (GaAs), Cadmium Telluride (CdTe), Copper Indium Diselenide (CIS) and amorphous silicon has proved to absorb photons much more readily than their indirect counter parts such as crystalline silicon. This is due to the lack of momentum that photons posses, resulting in solar cells becoming thinner [12]. The difference between direct and indirect bandgap materials, is that the k-vector in the Brillouin zone

(the difference between the lowest-energy state in the conduction band, and the highest-energy state in the valence band) are the same for direct bandgap, and different for indirect bandgap materials.

The basic working of solar cells stay the same. It is, however, factors such as the thickness of the devices, and absorption properties of the materials that drive new research into different materials and types of solar cells. Plastic solar cells for example, using organic and polymer materials, have the benefit of being much thinner and even flexible [13]. Grätzel or dye-sensitised solar cells use dyes to increase the absorption of photons, improving the efficiencies of solar cells drastically, but battling with stability [14]. Power conversion efficiencies are improved by using ingrain porous silicon sacrificial layers to randomise the surface morphology with etching to reduce reflection [15], or adding anti-reflection coatings [12].

2.4 Organic Solar Cells

When discussing organic solar cells, the terminology changes from a p/n junction as described in Figure 2.1, to a D/A (Donor/Acceptor) interface for a similar device. To achieve such a D/A interface two materials would be used, instead of using one and doping it as is done with inorganic Silicon devices. The big difference between organic and inorganic devices lie with the absorption of photons. Photons can be absorbed throughout the whole material, not just in the depletion region as in Si solar cells. Photons with energy equal to or higher than that of the excitation energy gap (band gap in silicon solar cells) will be absorbed. Due to small band sizes in organics, the excitation energy is represented by the energy difference between the HOMO (Highest Occupied Molecular Orbital) and LUMO (Lowest Unoccupied Molecular Orbital) of the material and not the VB and CB as in inorganics [5]. Once a photon is absorbed, Frenkel and not Wannier excitation occurs. This generates excitons or polaron-pairs, which are an electron hole pair with a neutral charge instead of free holes and electrons. Current flow is obtained when such an exciton reaches an interface where it can be separated into a free hole and electron, which needs to be extracted at an electrode. The distance that such an exciton can travel to an interface, where it is separated into a hole and electron, is known as the exciton diffusion length, and is a property of the material.

2.4.1 Organic Semiconductors

Table 2.1 shows a list of well know organic semiconductors. Two materials were chosen out of those to use in this project, namely Copper(II)Phthalocianine (CuPc) and Buckminster Fullerenes (C_{60}). Since one of the aims of this thesis is research into manufacturing as part of a nanotechnology group, these materials were preferred to others like P3ht, which might have superior absorption properties, because they are known as ENM's (C_{60}) which slows down charge recombination and accelerates photo induced electron transfer [16], or have shown interesting tendencies such as forming nanowires (CuPc) [2]. How these materials are used to make solar cells are discussed in Chapter 3.

Table 2.1: Organic materials that can be used as electron donor/acceptor semiconductors [5].

Donors or P-Type Semiconductor	Acceptors or N-Type Semiconductor
PBZT(D)	Perylenes
PPV	C_{60}
MEH-PPV	PCBM
MDMO-PPV	CN-PPV
RO-PPV-10	SF-PPV
PTh	BBL

2.4.2 Factors Influencing the Efficiency

As for inorganic photovoltaic cells, there are several factors that influence the performance of organic devices. In his review [4], Moliton lists six main factors to consider when designing an organic PV cell, as well as the three main areas associated with losses.

Design consideration:

1. Photon Absorption. Optical absorption coefficients of the organic materials, as for inorganic materials, differ with changes in the wavelength of the incident light.
2. Generation of excitons. Electron-hole pairs (excitons) with a neutral charge is generated when photons are absorbed, instead of free holes and electrons.
3. Exciton diffusion. Exciton diffusion has a large influence on the efficiency of the device. Excitons have a limited time and distance to move through the donor layer before recombining.

4. Exciton dissociation. If excitons reach a donor/acceptor interface, they can be separated into holes and electrons provided that the LUMO level of the acceptor is lower than the excitonic state at the bottom of the donor's conduction band.
5. Carrier transport towards the electrodes. The influence of transport to the electrodes on the efficiency of the device is normally considered negligible. The transport mechanism for organic materials is the hopping process. Traps reduce mobility, but are usually ignored.
6. Charge collection at the respective electrodes. Two conditions need to be met, in order to assume that the collection efficiency is equal to one. The work functions of the cathode and anode need to be smaller than the LUMO of the acceptor, and bigger than the HOMO of the donor respectively. This is most commonly achieved by designing exciton blocking layers into the device.

The causes for losses include:

1. Losses at the air-organic interface. Reflection is roughly 4% because the organic materials are more refractive, leading to the appearance of Fresnel losses.
2. Losses due to the diffusion of the incident radiation if the material is crystalline. This effect is ignored in organics, since organic materials are mostly amorphous.
3. Losses due to unabsorbed photons. Losses due to unabsorbed photons occur for two reasons. Firstly because of a mismatch between photon energy and the energy of the band gap. The same principles for absorption apply to organics. The second is insufficient layer thicknesses. If the material is too thin, the radiation will pass straight through without contributing to the exciton generation. If the layer is too thick, photons will be absorbed, but will still be lost since the distance is too far for the generated excitons to reach a D/A interface, and no dissociation will occur.

2.5 Conclusion

This chapter described the method of photo induced charge separation in general, as well as specifically for organic solar cells. In the next chapters, the focus will be to design a device that can achieve such charge separation, and especially, to get the exciton diffusion lengths correct.

Chapter 3

Design

This chapter looks at several layouts for organic solar cells. A design is then completed for a thin film device, starting with a simple layout, and then adding layers to it to increase the performance. The construction of the designs shown in this chapter is described in Chapter 4.

3.1 Configurations of Organic solar cells

3.1.1 Schottky type Single Layer Solar Cells

Single layer or MIM (Metal-Insulator-Metal) photovoltaic cells are made by sandwiching a semiconductor material between two electrodes. The top electrode needs to be transparent, typically ITO, and the bottom electrode needs to be reflective, typically aluminium or silver. MIM devices have poor performance recordings mainly due to the only slight difference in internal potential, given by the difference in work functions of the metals

$$W_{int} = W_{anode} - W_{cathode}. \quad (3.1)$$

This low internal potential difference leads to a low dissociation efficiency of photo-generated excitons of about 10 % [4].

3.1.2 Blended or Bulk Heterojunction

Blended heterojunction solar cells are devices where more than one material is used for photo absorption. The materials, a donor and acceptor, are mechan-

ically mixed and evaporated or co-evaporated to form a single layer between electrodes. The main advantage of a mixing layer is that layer thickness can be increased, which increases photo-absorption. The main disadvantage lies with the manufacturing, in that it is difficult to control the donor and acceptor paths in the layer. The mixed layer has the advantage that the distance to a donor/acceptor interface can be kept small, but the disadvantage that both the donor and acceptor could make contact with either or both electrodes.

3.1.3 Heterojunction

A heterojunction or bi-layered device consists of two or more materials layered on top of one another. The bi-layered device has shown the best compromise between manufactureability and efficiency. Therefore it was chosen as the focus of this thesis, and the design is discussed further in Section 3.2.

3.1.4 Nanostructured or Nano-ordered Solar Cells

The real challenge for nanotechnology in photovoltaic cells lies with the nano-ordered device. The nano-ordered device is a combination of the bi-layered and bulk heterojunction devices. A representation of such a device is shown in Figure 3.1. As can be seen in Figure 3.1, a layer of donor acceptor fingers are sandwiched between a donor and acceptor layer. To get the optimal efficiency out of such a device, the top and bottom layer's thickness should be equal to the exciton diffusion length of the materials, and the fingers should be as long as possible while their widths should be kept at the exciton diffusion lengths of the respective materials.

The design is similar to a p-i-n construction in inorganic photovoltaics, where the fingers are inserted to increase the D/A interface and thicken the photo absorption length, while keeping the exciton diffusion length as short as it would be in a bi-layered device.

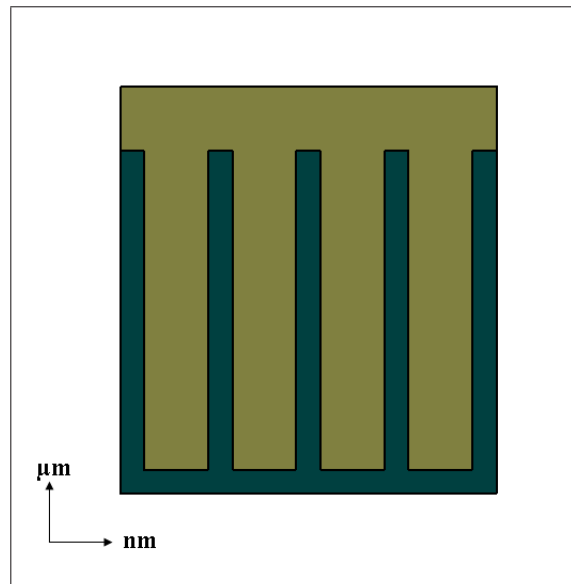


Figure 3.1: Nanostructured PV cell. A representative layout of a nanostructured solar cell. Nano fins extend upwards to create a thicker cell for absorption, while keeping the widths down to exciton diffusion lengths in the nanometer scale.

One possible way to achieve this design is through nanolithography. AFM scratching would also be able to scratch 40 nm lines, but it would not be possible to do it over large areas, as the case is with lithography. Currently, there are three techniques to do nanolithography, as reported by Zhou [17]:

- Electron Beam Lithography (EBL)
- X-ray Lithography (XRL)
- Extreme Ultraviolet Lithography (EUVL)

Current optical lithography is limited to a resolution of 250 nm using ultraviolet light with a wavelength of 248 nm. In EUVL, UV light at a wavelength of 193 nm is used, and the light is reflected from mirrors rather than refracted through lenses, to achieve a maximum resolution of 130 nm.

Electron beam lithography is achieved by focussing the electron beam on a photo sensitive material. Typically a negative photoresist would be used, such that the pattern drawn would stay behind after development. Figure 4.2 summarises the difference between positive and negative lithography. The resolution of EBL is limited by the focus of the beam, and as with the AFM, the area is smaller than the size required for PV applications as well.

X-ray lithography, despite its higher cost, is a very attractive option to nanofabrication. This is due to the short wavelengths of interest for x-ray lithography, between 0.5 nm and 4.5 nm. XRL is of interest for resolution in the single digit nanometer range, by eliminating problems associated with depth of focus, reflection and scattering [17].

3.2 Bi-layer or Heterojunction

3.2.1 First Device

The first design for the bi-layer device is shown in Figure 3.2. It is a simple structure made by layering two organic semiconductors on top of a TCO (Thin conducting oxide) layer. The silver strips are placed as contacts to extract current. CuPc and C_{60} were used as the P/N or Donor/Acceptor materials respectively, with exciton diffusion lengths assumed, as indicated for the first design. Both semiconductors and the ITO glass used were obtained from Lumtec (Luminescence Technology Corp.) in Taiwan. The ITO glass was supplied in 25 mm by 25 mm squares, 0.7 mm thick with no patterning (glass is completely covered with ITO).

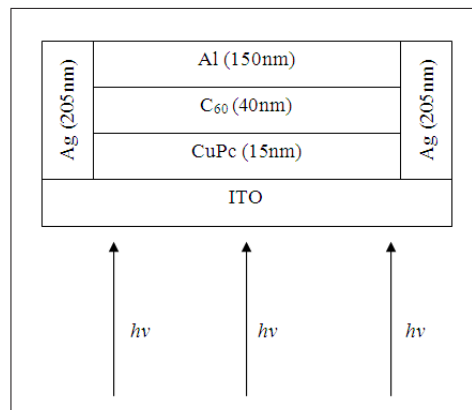


Figure 3.2: First device layout. First design of an organic solar cell. Two semiconductor layers sandwiched between electrodes as donor and acceptor layers.

3.2.2 Pyramid Layout

The second design is a change of the first, after testing revealed a short circuit in the first design. As can be seen in Figure 3.3, this design is such that all the

materials (not including the silver), is deposited in a square, smaller than the material that precedes it, thus forming a pyramid shape.

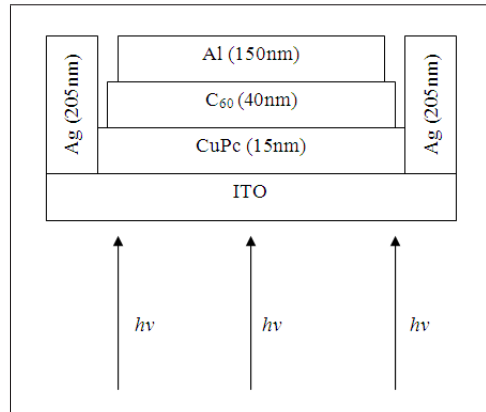


Figure 3.3: Pyramid shaped solar cell. Layers following the CuPc are made smaller to represent a pyramid form, to avoid overlapping at the edges.

3.2.3 Adding EBL

The first layer added to try and improve the efficiency of the device, was BCP. As seen in Figure 3.4, the BCP layer was added while continuing with the pyramid scheme. The energy level of the cathode, the aluminium layer, is preferred to be lower than the LUMO of the acceptor (C_{60}) layer. As can be seen in Figure 3.6, the BCP has a LUMO of 3.5 eV, were as the C_{60} with 4.5 eV is slightly higher than the aluminium (4.2 eV). As reported by [18], the BCP now transports the electrons from the adjoining acceptor layer to the aluminium, while effectively blocking excitons in the acceptor layer from recombining at the cathode.

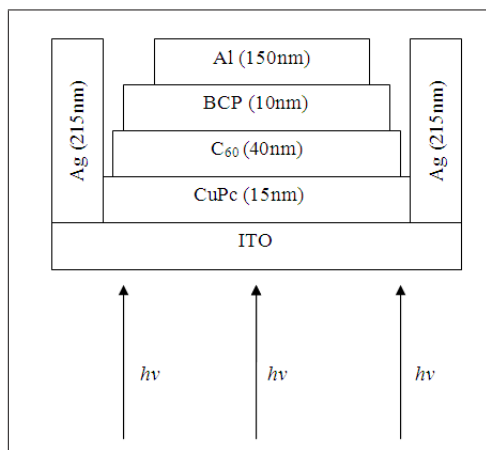


Figure 3.4: Solar cell with BCP added as an exciton blocking layer.

3.2.4 Adding PEDOT:PSS

The second layer added to improve the efficiency of the device was PEDOT:PSS. The PEDOT as will be explained in Chapter 4, is spun on beforehand, and thus covers the entire sample.

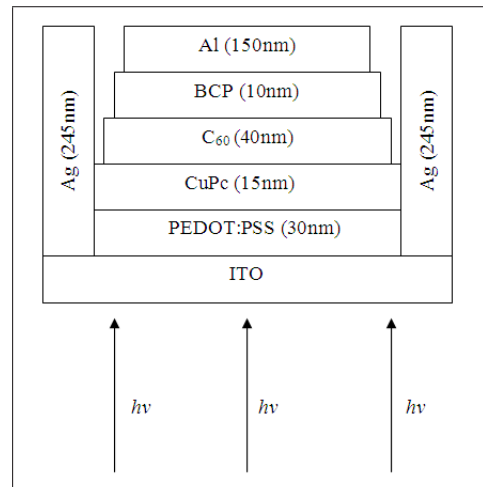


Figure 3.5: Solar cell with PEDOT:PSS added. A representative layout of a complete heterojunction solar cell with BCP and PEDOT:PSS as exciton blocking layers.

The reason why PEDOT should improve the efficiency of the solar cell, as reported by [18], is that the energy level of the anode (ITO) must be bigger than the HOMO of the donor (CuPc). The PEDOT buffer, or exciton blocking layer, reduces the potential barrier at the ITO interface, as shown in Figure 3.6. This results in better hole extraction (by preventing exciton recombination) and thereby a higher efficiency in the device.

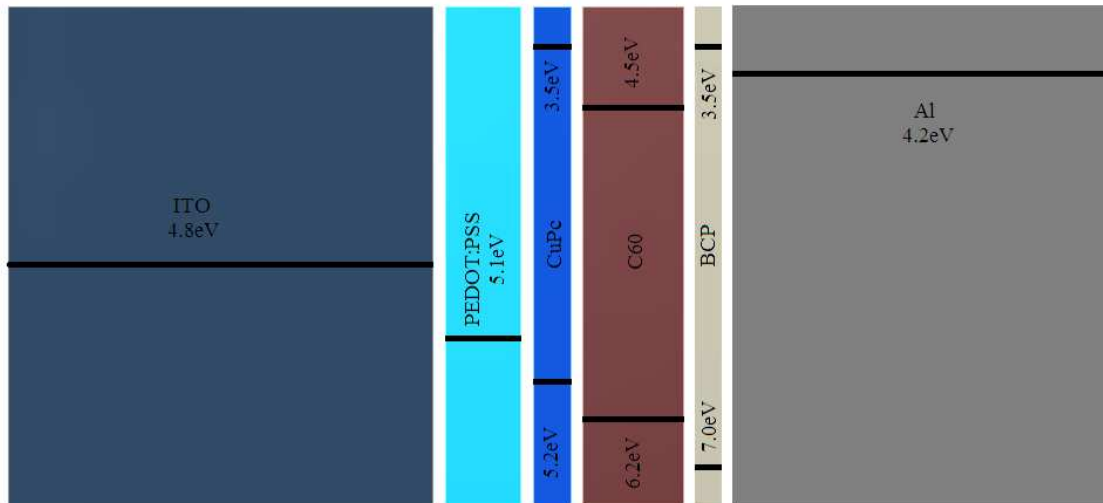


Figure 3.6: Energy diagram showing the energy level matching between exciton blocking layers and the HOMO and LUMO of the semiconductor materials.

3.2.5 Nanowires

According to [2], heating the substrate during CuPc deposition on gold, creates horizontal nanowires as shown in Figure 3.7. These results were obtained on silicon samples, which have a crystalline structure. To investigate the effect that CuPc nanowires could have on the efficiency of the cell, sample temperatures can be increased between 0 °C and 200 °C during the CuPc deposition. The change in temperature shows a change in CuPc nanowires construction, which could influence solar cell efficiency.

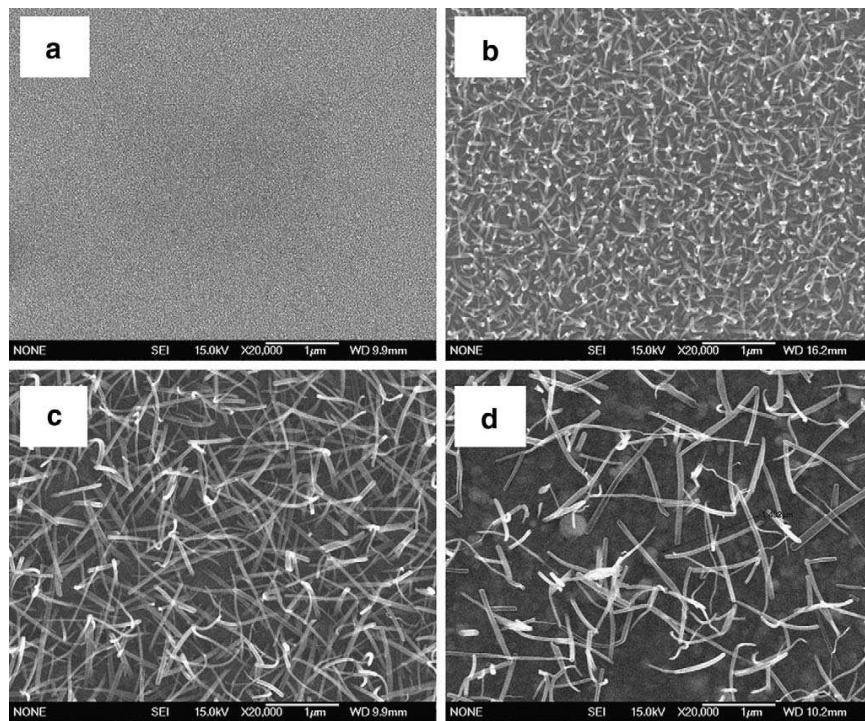


Figure 3.7: SEM images of CuPc layers deposited on Au substrates at various temperatures:(a) room temperature, (b) 100 °C, (c) 150 °C and (d) 200 °C [2].

3.3 Conclusion

Even though it is possible to do lithography down to the 15 nm resolution required to make a CuPc/C60 D/A nanostructured photovoltaic cell, stretching that to even the small sample sizes of 25 mm used in this project, is a new science all together. The restriction on lithography techniques again motivate the design of heterojunction solar cells for this project.

Chapter 4

The Manufacture of TFOSC

This section describes how the thin film organic solar cells designed in Chapter 3 were manufactured. All the steps are shown, including manufacturing techniques used and how materials were calibrated to be the correct thickness. This chapter also outlines more than one method of material thickness calibration, using the AFM.

4.1 Equipment & Techniques

Thermal Evaporation is a process to deposit material onto either a cold or heated sample under vacuum. The material is evaporated by resistively heating it in a crucible. Crucibles are typically made from tungsten or other materials with very high melting points, such as tantalum or molybdenum. The thermal evaporator was modified for this project, making a module that could bolt onto the base. This allowed for eight additional wires to enter the vacuum chamber. Four wires were used to drive the two heating elements in the sample heater, and four was used for thermocouples. The first thermocouple was used as feedback for the sample heater controller. The second thermocouple was placed underneath the tungsten crucible, to measure the source temperature during deposition. The thermal evaporator used, is shown in Figure 4.1.



Figure 4.1: Thermal Evaporator situated in the cleanroom.

Spin Casting is a technique used to deposit liquid materials on samples at various thicknesses. Samples are placed on a spinning disk and held in place by a vacuum chuck. The material can be dispensed onto either a stationary or rotating sample. The volume of the liquid deposited decreases with an increase in time and speed, because of radial flow caused by centrifugal forces as describe by [19]

Sputtering is a method of thin film deposition, using a DC glow discharge under low vacuum pressures of carrier gas, to create a plasma between a source material and a substrate. The mean velocity of the atoms arriving at the substrate (as a result of accelerated ions dislodging atoms from the source material), is much higher in sputtering methods than in thermal evaporation [20].

Lithography means the pattern transfer to a photosensitive material by selective exposure of a substrate to a radiation source [21]. Photolithography was used in this project with an ultraviolet light source. Figure 4.2 demonstrates the difference in mask layout in using a positive and negative photoresist.

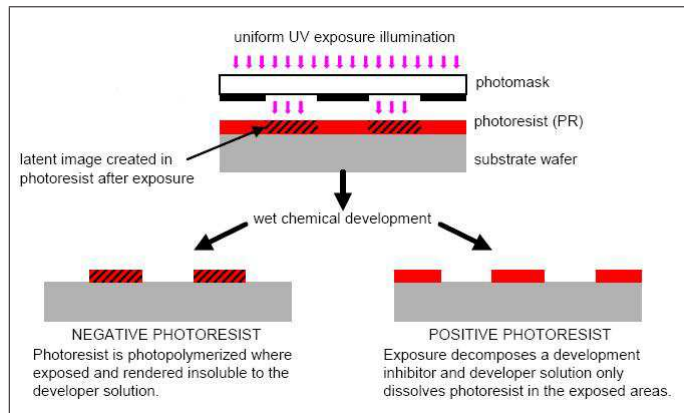


Figure 4.2: Photolithography exposure process. Ultraviolet light penetrates the gaps in the mask and chemically alters the photoresist [22].

The Atomic Force Microscope, shown in Figure 4.3, was extensively used in thickness measurements throughout this project. Briefly put, the Atomic Force Microscope consists of a very small cantilever which moves over a sample surface, and measures the surface height by measuring the cantilever deflection through laser reflection and photo diodes. It is of key importance to calibrate the AFM before using it in applications where tolerances are very important, i.e. a thickness tolerance of ± 1 nm, or after changing tips. It was found in this work that a non-contact tip delivered the most accurate results for step and thickness measurements. Other tips such as contact tips, had more noisy signals. This made it difficult to do fine measurements. To calibrate the AFM, the micro structure, as shown in Figure 4.4, should be scanned first, and the PI controller values tweaked until the specified depth of 98 nm for the holes are obtained.

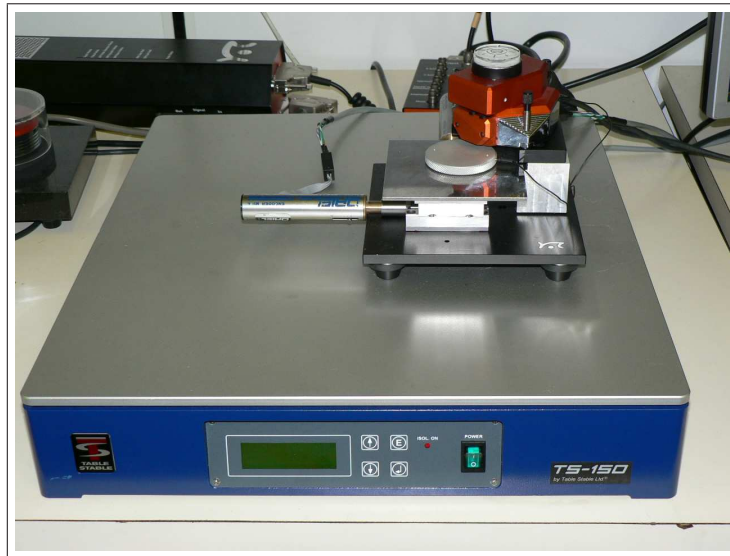


Figure 4.3: Atomic Force Microscope as set up in the cleanroom, on the Table Stable to reduce interference from external vibrations.

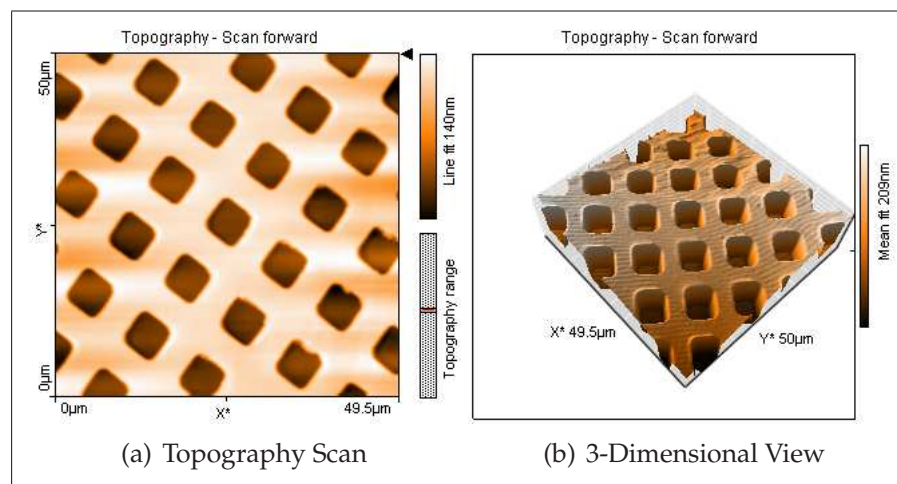


Figure 4.4: AFM micro structure scanned to calibrate the AFM controller values. The structure has a depth of 98 nm in the Z-direction, and a periodicity of 10 μm in the XY-directions.

4.2 The first Design of an Heterojunction cell

In the first design described in Section 3.2.1, four materials were used and deposited on ITO glass through masks one and two, which is shown in Appendix A. The silver was deposited through mask 1, and the rest of the materials through mask 2. As can be seen in the design, these materials need to be a specific thickness. The calibrations were done as described in the following sections.

4.2.1 Heterojunction materials

Since the exciton diffusion lengths of CuPc and C₆₀ are 15 nm and 40 nm respectively as reported by [23], a QCM sensor was used to ensure that the correct film thicknesses could be deposited. The correct QCM setup values first needed to be determined for each material. This was done with an iterative method of material deposition and thickness measurement with an AFM. A pattern with square blocks was created on polished MgO samples using AZ5214 as a positive photo resist, as can be seen in Figure 4.5. One drop of the AZ5214 was dripped onto each of the MgO substrates, which were cleaned with acetone in an ultrasonic bath, and spun for 30 sec at 6000 rpm to ensure even, thin and smooth films. The substrates were then pre-baked for 1 min on a hot plate at 95 °C. The samples were then exposed for 25 sec to ultraviolet light under a mask to form the pattern in Figure 4.5. The samples were then placed in a developer for 1 min and blow dried with Nitrogen.

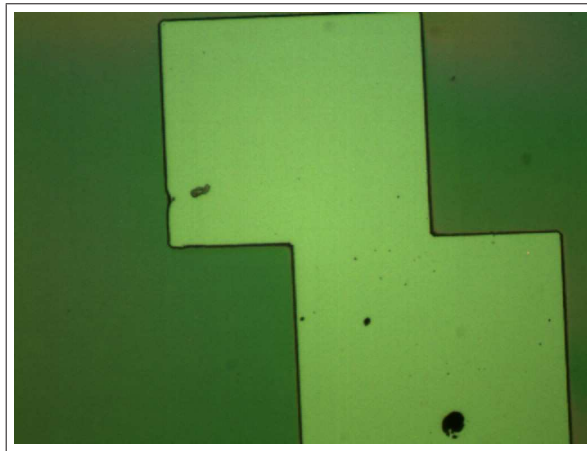


Figure 4.5: Photoresist blocks on a polished MgO sample.

The initial values for the three QCM factors were set as: Tooling - 110 % as the sensor is mounted higher than the sample holder. Density - 1620 kg/m³ for CuPc [24] and 1720 kg/m³ for C₆₀ [25], which will stay fixed for the duration of the iteration. The initial Z-factors were calculated as 15 for CuPc and 3.45 for C₆₀ from

$$z = \sqrt{\frac{D_q \times U_q}{D_m \times U_m}} \quad (4.1)$$

where D_q and D_m respectively represents the densities of quartz (2643 kg/m^3) and the deposited material. U_q and U_m respectively represents the shear modulus of quartz (32 GPa) and the deposited material. For the C_{60} Equation (4.1) could be applied directly since the values for the density (1720 kg/m^3 [25]) and shear modulus (4.14 GPa [26]) could be obtained. For CuPc the density is known, but the shear modulus was approximated to be 3.4 GPa from

$$G = \frac{E}{2(1 + \nu)} \quad (4.2)$$

In Equation (4.2) the Poisson's ratio (ν) was set to that of Cu (0.36). The Young's modulus, E , was taken as 9.29 GPa [27].

All the physical vapour deposition of the sublimation materials were started and maintained at a vacuum pressure of more than $2.6 \times 10^{-5} \text{ mbar}$. The materials were then deposited onto the MgO samples until the QCM sensor read 50 nm . The materials were evaporated by resistively heating a tungsten boat. The temperature was slowly increased over a 20 min period before the shutter was opened, in order to allow any impurities (moisture) to dissipate. The optimal temperatures for a steady evaporation rate was found to be $580 \text{ }^\circ\text{C}$ for the CuPc and $650 \text{ }^\circ\text{C}$ for C_{60} . After deposition the samples were dipped into an acetone bath for approximately 1 min until all the photo resist lifted off. The samples, left with only small squares of deposited material, as can be seen in Figure 4.6, were then taken to an AFM.

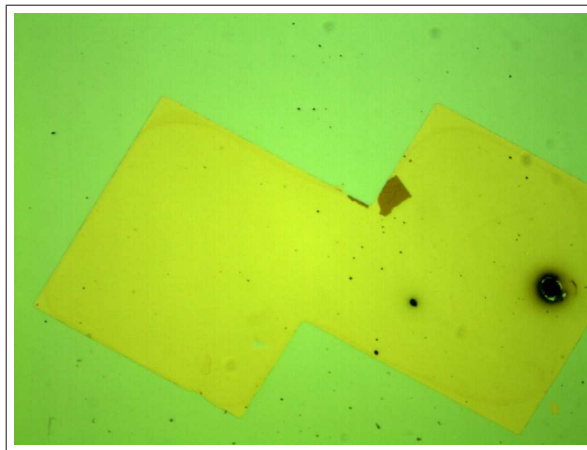


Figure 4.6: CuPc left on MgO after liftoff in acetone.

The tip of the AFM was positioned over the edge of each square, as can be seen

in Figure 4.7. The area around the step is then scanned to obtain figures such as Figure 4.8. A cross section is taken with the software to obtain Figure 4.9, from which the thickness of the deposited material can be read. Several scans should be taken of various steps on the sample, and measurements averaged to ensure that an even film thickness was deposited and the correct reading is obtained, removing faults resulting from poor manufacturing (lift-off).

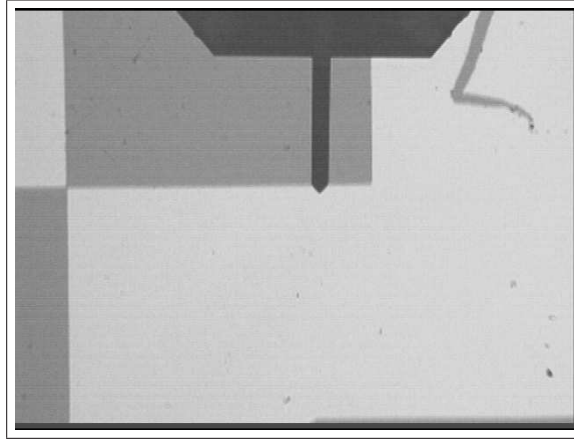


Figure 4.7: The tip of the AFM is positioned over the step formed by the deposited material on the MgO sample.

The actual measured thicknesses for each material can then be fed into Equations (4.3) and (4.4) to obtain the new parameters for the QCM sensor. In Equations (4.3) and (4.4), T_1 is the thickness indicated by the QCM sensor and T_2 is the thickness measured by the AFM. This process is then repeated until the values from the QCM sensor and the AFM are equal.

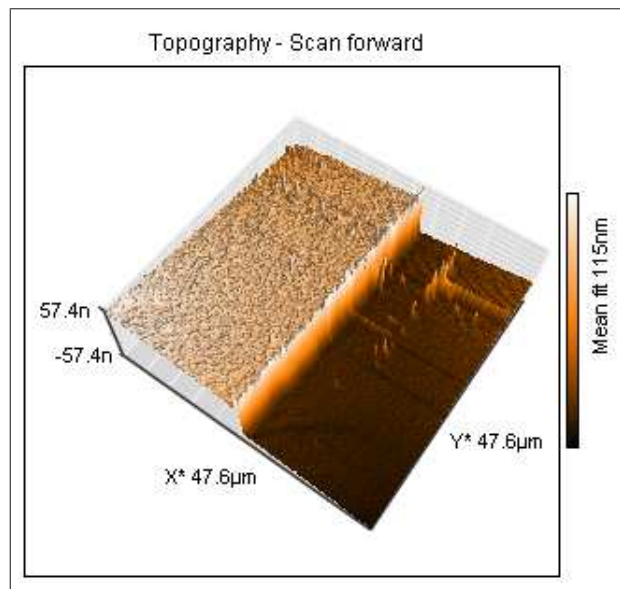


Figure 4.8: A 3-dimensional view of a scan done over the edge of the deposited material. This step edge is used to measure the thickness of the deposited material.

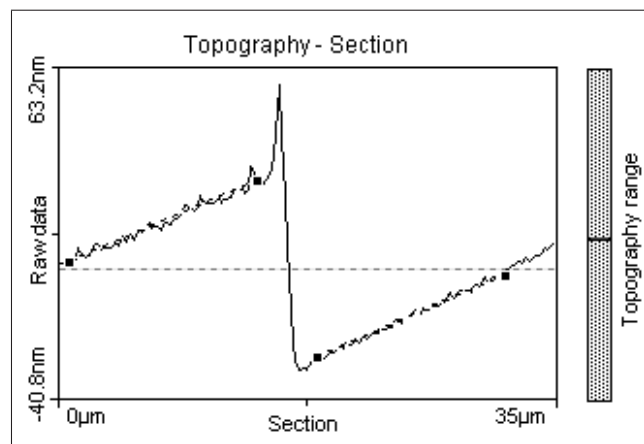


Figure 4.9: Cross section of the step edge is created by the software in order to use the distance measuring tool.

The equations to calculate the new tooling factor and Z-factor is given as

$$Tooling_{new} = Tooling_{old} \times \frac{T_2}{T_1} \quad (4.3)$$

and

$$Z_{new} = Z_{old} \times \frac{T_1}{T_2}. \quad (4.4)$$

4.2.2 Metal electrodes

For the electrodes, two metals were used, namely Sterling Silver and Aluminium. Both materials were thermally evaporated, and its thicknesses controlled with QCM sensors. Calibrating the sensors for the metal electrodes is easier than that of the organic materials, since the density and acoustic impedance values are given in the data sheet for commonly used materials. Thus it is only necessary to determine the correct tooling factor. Since a much thicker metal layer is deposited, a new crystal was used for each material, as lifetime loss is much more prominent. Lifetime loss on QCM crystals should be monitored closely, as a drop in 10% necessitates recalibration of the tooling factor to keep the deposition rate monitoring accurate. A new tungsten crucible was also used for each new material used in the thermal evaporator, in order to keep contamination as low as possible.

4.3 Pyramid Heterojunction

After the completion of the design described above, it became clear that each material will need its own mask. The reason is twofold: firstly, the materials vary in thickness from 15nm to 150nm, and secondly there is a vibration from the vacuum pump on the thermal evaporator. Therefore it is impossible to create a structure where more than one material is being deposited through the same shadow mask to line up perfectly as illustrated in Figure 3.2. The net result in this case being that the aluminium drifts over the organic materials and contacts the ITO, creating a short circuit.

Two more masks were thus added. The dimensioning can be seen in Appendix A, in Figures A.4 and A.5. Table 4.1 summarises which mask was used with which material to create the structure illustrated in Figure 3.3.

Table 4.1: Shadow masks used to create a pyramid structured solar cell through thermal evaporation.

Material	Masks number	Reference
Silver	Mask 1	Figure A.2
CuPc	Mask 2	Figure A.3
C ₆₀	Mask 3	Figure A.4
Aluminium	Mask 4	Figure A.5

As mentioned in the design section, the organic semiconductor materials have exciton diffusion lengths. It was reported that one possible way to determine these thicknesses was by means of photo luminescent (PL) quenching [18]. These experiments are difficult to replicate, and the facilities needed are not available at the university. Thus it was decided to determine the thicknesses by trial and error.

The assumed exciton diffusion lengths for CuPc and C₆₀ were 15nm and 40nm respectively as reported by [28] and [29]. However, to ensure that this holds true for the materials obtained from Lumtec, several variations of the 15/40 hetero-junction were made and tested, to see which thickness combination gave the best results. See Chapter 5 for these results.

4.4 Adding Exciton Blocking layers

4.4.1 Calibration of BCP

BCP or Bathocuprione was chosen as an exciton blocking layer between the C₆₀ and aluminium cathode. BCP was obtained from Sigma-Aldrich, and it is also a sublimation material. It was reported that the BCP thickness needs to be 10nm, to avoid adding too much resistance to the device. However, calibrating the BCP layer added some challenges.

The same method of calibration for the deposition rate of BCP was used as that of the organic layers. A sample with a photoresist mask was prepared in the same way as described in Section 4.2.1. However, very little information about the density and acoustic impedance of BCP is readily available, requiring a new approach to be taken. A new QCM sensor was used, as not to use lifetime on the other sensors used for the organic materials. The tooling factor was started at 300, and the density and z-factor made one. This meant that several more iterations of deposition and measurement with the AFM was necessary, correcting all three factors using Equations (4.3), (4.4) and (4.5). The result, however, was the same in that the sensor could be calibrated to measure the BCP thickness to within one nanometer.

$$Density_{new} = Density_{old} \times \frac{T_1}{T_2} \quad (4.5)$$

There were, however, two more challenges. Firstly the deposition temperature, and secondly the liftoff. The deposition or source temperature needed for BCP, was found to be less than 200 °C. And since a large amount of current is sent through the tungsten crucible (for evaporation of metals) in the thermal evaporator, the variac sensitivity is only 10 A. The result being that a small turn in the variac for less and more current, was the difference between zero deposition, and a rapid deposition rate of more than 60 Angstrom per second, forcing the BCP powder to rapidly spill out of the crucible before the shutter could be opened. This was rectified by using more than one crucible. A second crucible was used to hold the BCP, but was electrically insulated from the previous crucible by placing ceramic spacers in between. This meant that current was only flowing through the bottom crucible and that the small amount of convection heat transfer through the 1mm gap, heated the crucible holding the BCP.

Once the deposition problem was solved, it was found that liftoff with a photoresist mask could not be obtained. The reason for this is that acetone and ethanol dissolves the deposited BCP faster than the photoresist. Figure 4.10 shows an optical image taken from one sample dipped in photoresist remover, diluted in a one to one ratio with de-ionised water. As can be seen, the layer was still severely damaged and no step could be measured on the AFM.

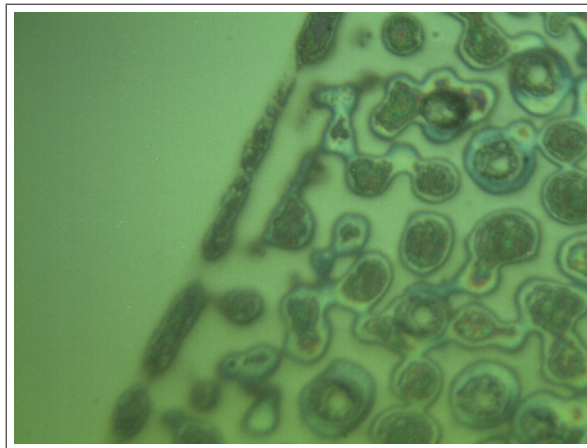


Figure 4.10: Leftover BCP after liftoff in diluted photoresist remover.

This meant that an entirely new solution was needed. The reason photoresist masks are used for liftoff, is mainly because the photoresist sticks nicely to the polished samples, so that no material can deposit underneath the edge. This is the main reason why using something like masking tape does not work. The principle is illustrated in the solution to the BCP liftoff using Rubylith films. Fig-

ures 4.11 and 4.12 shows two optical images of BCP deposited onto polished silicon, which were partly covered by Rubylith films. Figure 4.11 shows the sample where Rubylith was stuck onto polished silicon to try it for liftoff. It shows that even for a thin material such as Rubylith, there is a gap between the silicon and the Rubylith film where the BCP penetrated. As seen by the dimensioning in Figure 4.11 the result is an uneven step edge of around 50 μm thick. It is thus impossible to measure the thickness of the BCP over that step using the AFM, since the largest scan size of the AFM is 50 μm .



Figure 4.11: BCP film as seen under an optical microscope when using Rubylith to create a step edge. An uneven step was created as can be seen in the transition from the dark area (BCP) to the light area (polished sample).

However, sticking rubylith onto the polished silicon sample and heating it up on a hotplate at 90 °C for 1 min forces the air trapped between the silicon and Rubylith to escape and the thin Rubylith film to shrink onto the sample. Depositing BCP on a sample prepared in this manner, results in Figure 4.12, when looking under the optical microscope. As can be seen, a much smoother edge was obtained and the thickness could be measured, allowing for the BCP deposition rate to be calibrated successfully.

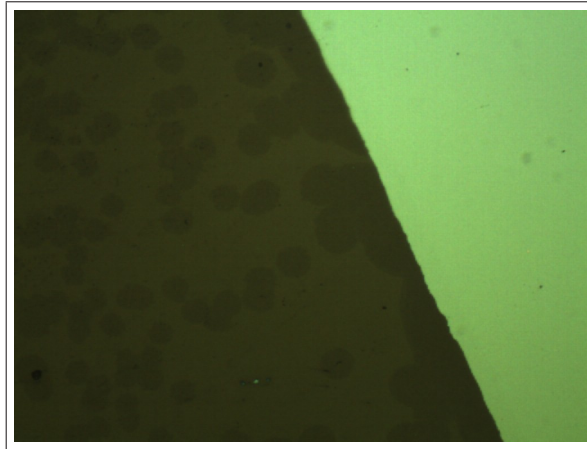


Figure 4.12: The improvement in the BCP step edge from a heating the Rubylith as seen under an optical microscope. The change in colour is due to the lighting of the optical microscope.

As BCP is also thermally evaporated, a new shadow mask was made to keep the form of the pyramid going. The dimensioning for the mask, called mask 5, is shown in Figure A.6, and Table 4.1 is updated here to Table 4.2, listed in order used, to avoid confusion.

Table 4.2: Shadow masks used to create a pyramid structured solar cell through thermal evaporation, listed in order used.

Material	Masks number	Reference
Silver	Mask 1	Figure A.2
CuPc	Mask 2	Figure A.3
C ₆₀	Mask 3	Figure A.4
BCP	Mask 5	Figure A.6
Aluminium	Mask 4	Figure A.5

4.4.2 Calibration of PEDOT

PEDOT:PSS was used as a buffer layer between the ITO and CuPc. As for all the other materials used, it is important to control its thickness. Unlike the other materials, PEDOT was not thermally evaporated. PEDOT:PSS was obtained from Sigma Aldrich in liquid form, and was used as is. The liquid was spun onto the samples using spin casting.

To calibrate the thickness of the PEDOT layer is a very daunting task. There are only two variables that can be controlled during spin casting, namely spinning speed and spinning time. The reported optimal thickness for PEDOT is

30 nm [18]. To achieve this thickness, the correct speed and time needed to be determined. Firstly a 100 μl pipette was obtained from the department of Microbiology, in order to minimise material waste, and to ensure that the same amount of liquid was dripped onto the sample during each iteration.

There were a number of challenges in measuring the thickness of the PEDOT. Firstly, no mask could be used on the sample since it would interfere with the PEDOT spinning onto the sample. Secondly, the ITO glass has a surface roughness of about 40 nm. It would therefore be pointless to calibrate the spinning time and speed on a polished silicone sample, as it would not result in the same thickness on the ITO glass. Thus the ITO glass was used for calibration, and its surface roughness makes it difficult to measure a neat step with the AFM. Another difficulty is the PEDOT's viscosity. PEDOT needs to be stored at a temperature below 8 °C. This means that when using it, its temperature slowly rises to room temperature, changing the viscosity.

To start off, a spinning speed of 4000 rpm and a time of 40 sec was used as proposed by [18]. The second method of spin casting i.e. spinning before dripping the material was used. The second method was preferred to reduce material waste, as the vacuum chuck has a high initial velocity, and the PEDOT has a very high viscosity, a lot of material needs to be used to cover the whole sample. While spinning the sample and then dripping the material, a 100 μl proved an adequate amount. After spinning on the material, the sample was baked on a hotplate at 150 °C for 40 min. Several different methods were then used to try and determine the thickness.

Using the diamond tip scratching tool used to cut silicon wafers, a cross was made on the backside of the ITO glass. The cross can be seen in Figure 4.13, showing how it was used to position the tip of the AFM. This was done to do a surface roughness comparison before and after spinning, and using the AFM to scan at roughly the same position.

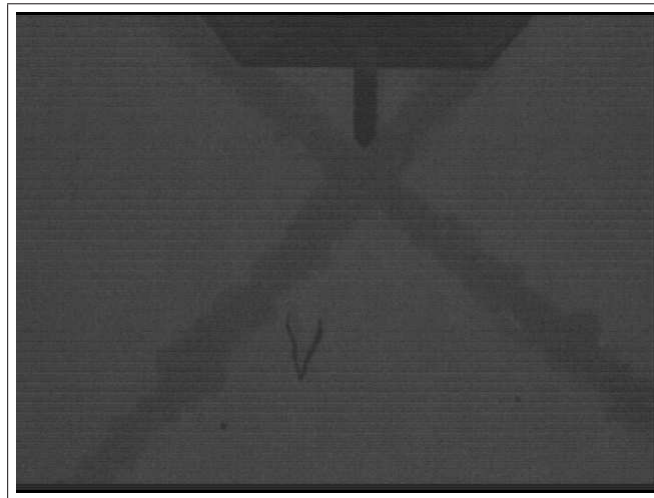


Figure 4.13: AFM tip positioning over a cross on ITO glass.

Since the ITO has a surface roughness, the aim was to spin on the PEDOT until a 30 nm improvement could be seen in the surface roughness. Figures 4.14 and 4.15 shows the surface roughness before and after spinning, measured at the same place as indicated by Figure 4.13. Using the Nanosurf software, an area roughness could be made of the scan. Figures 4.14 and 4.15 are screen shots of this application in the Nanosurf Easy Scan software. The values of importance are the S_y values, which indicate the height difference between the lowest part or valley and the highest part or peak in the area.

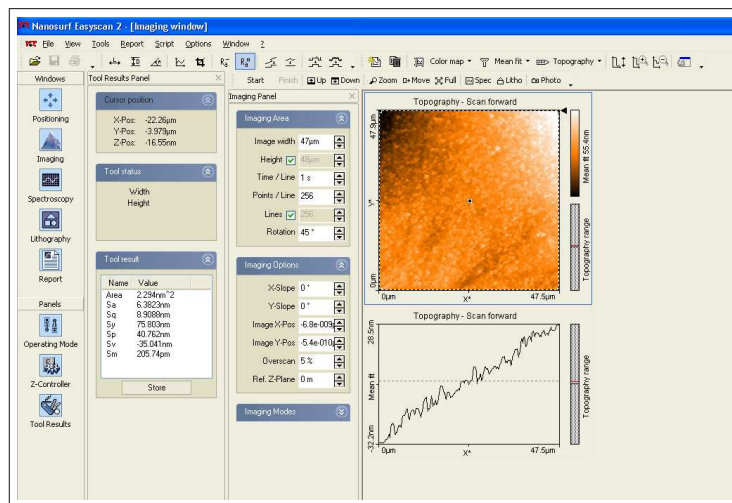


Figure 4.14: Surface roughness of ITO on glass as measured with the AFM over the cross made on the backside. Surface roughness as indicated by the peak-valley distance is 75 nm.

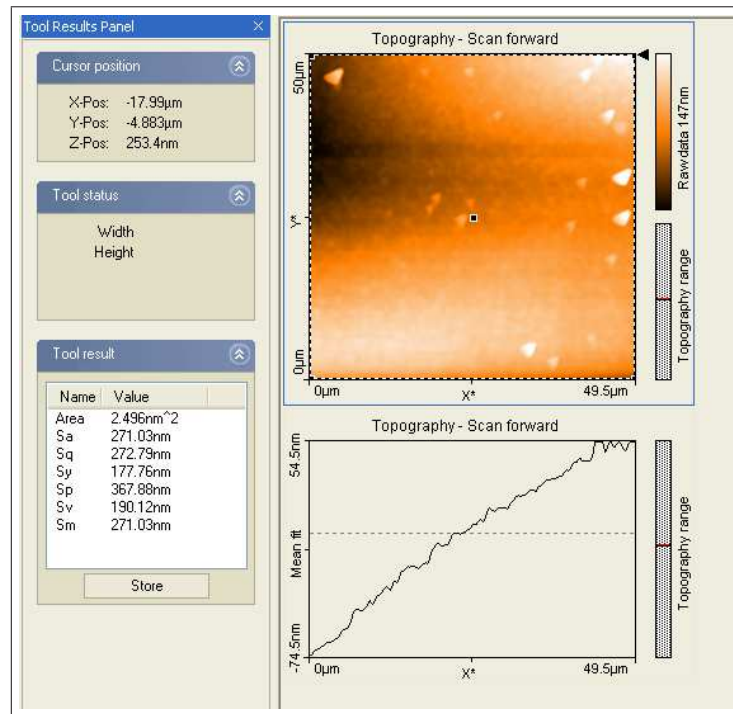


Figure 4.15: Surface roughness of ITO on glass after adding PEDOT:PSS as measured with the AFM over the cross made on the backside. Surface roughness as indicated by the peak-valley distance is 177 nm, unexpectedly worse than before adding the PEDOT.

As can be seen in Figures 4.14 and 4.15, instead of an improvement in surface roughness, it has gone worse. This result is deceptive, as can be seen in Figure 4.16, which has a smaller scan area. Figure 4.16 shows that the surface roughness has smoothed, and that it appears worse because of spikes on the scan. These spikes could be attributed to dust collecting on the sample during the 40 min baking of the sample after spinning.

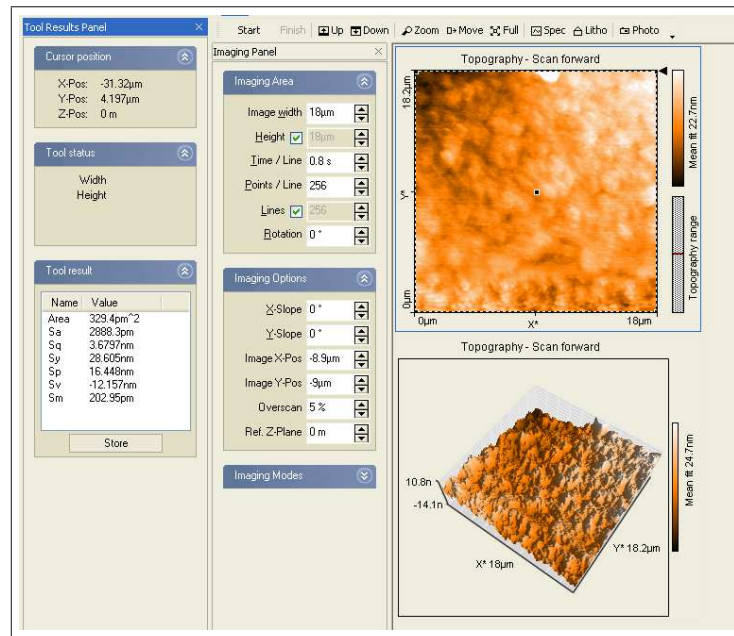


Figure 4.16: Surface roughness of ITO on glass after adding PEDOT:PSS, zoomed in on a smaller area, shows the improvement in that the peak-valley distance is actually 28 nm.

Another method of measuring the thickness was done by cutting a line in the PEDOT film using a scalpel blade. Figure 4.17 shows the scan made by the AFM over the cut, and Figure 4.18 shows one of the steps measured. The problem with this method is the non uniformity of the depth of cutting.

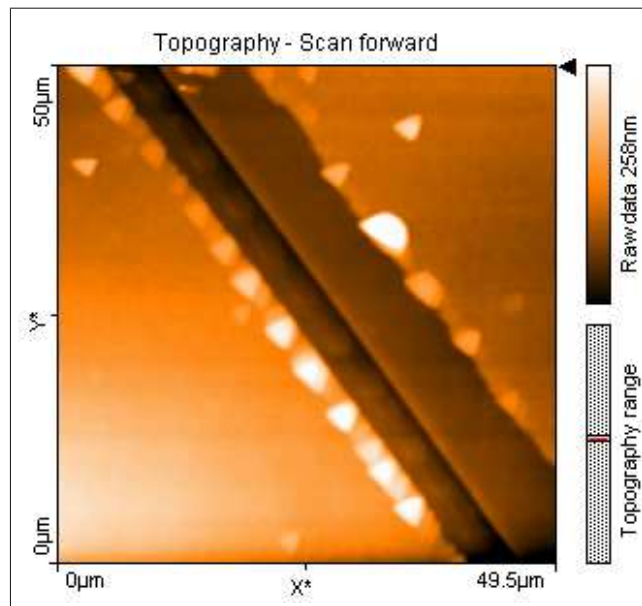


Figure 4.17: Topography scan of the cut made in the PEDOT layer with a surgical blade. The surgical blade was used to cut through the PEDOT onto the ITO in order to determine the PEDOT thickness with the AFM.

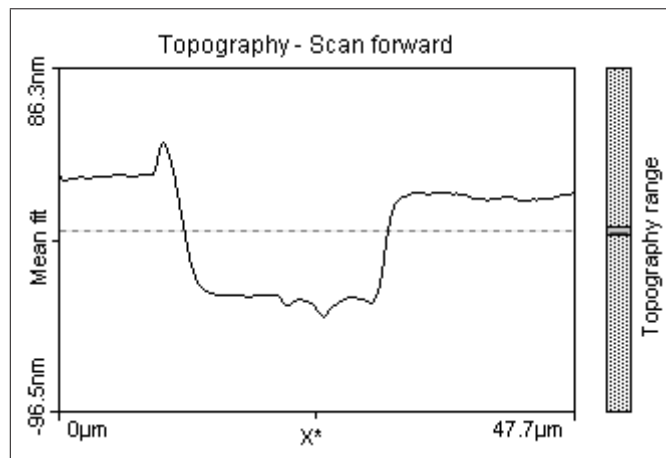


Figure 4.18: Cross section of a cut made in PEDOT to measure the depth.

The last option, which worked the best, was scratching through the PEDOT with the AFM. In the lithography package of the Nanosurf software, a line as shown in Figure 4.19 was scratched on the sample, using a silicon tip and a force of 200 nN. The scratch was made 5 times, to ensure that the AFM scratched through the PEDOT layer and removed the material out of the trench. The thickness of the film was obtained by scanning over the scratched line, measuring depth instead of a step height. Figures 4.20 and 4.21 show a three-dimensional view and the depth measurement scan respectively.

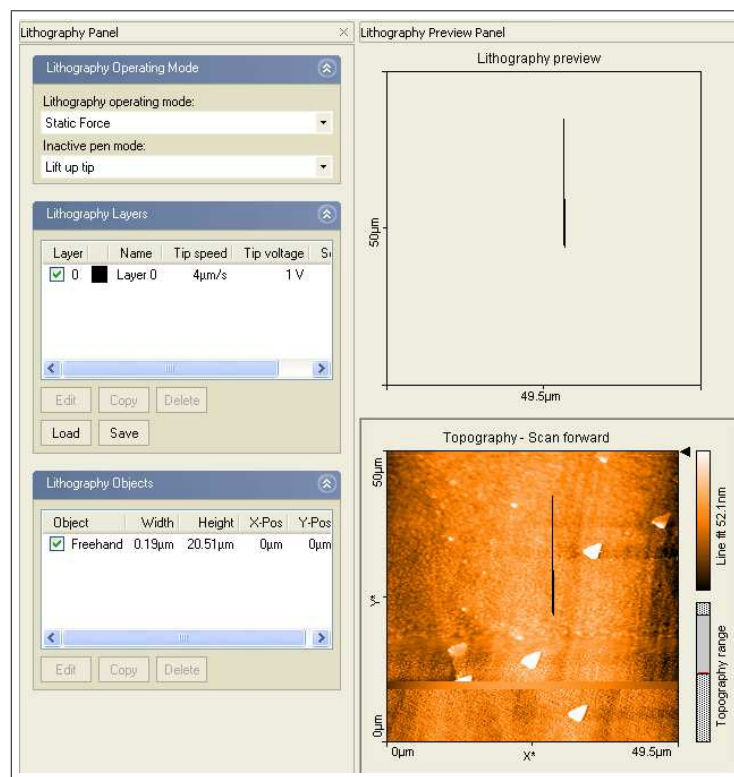


Figure 4.19: Lithography setup used with a contact tip to scratch a line through the PEDOT layer. A line was drawn in freehand mode to be 20 μm long and 0.19 μm thick.

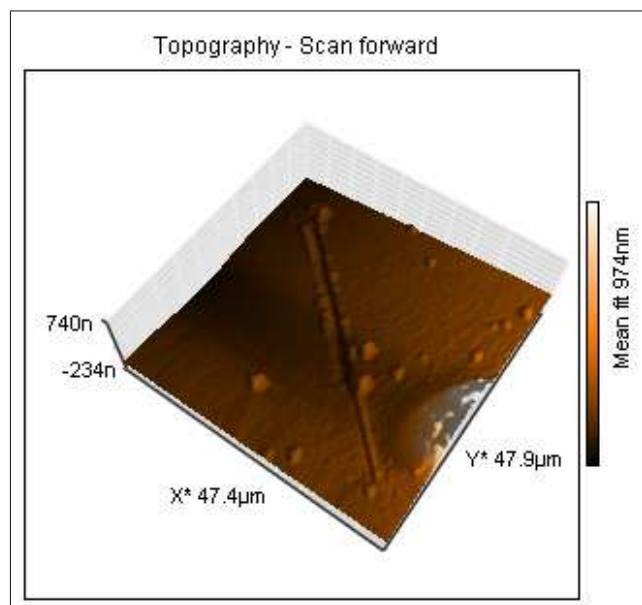


Figure 4.20: A 3-dimensional view of the line the AFM scratched into the PEDOT layer.

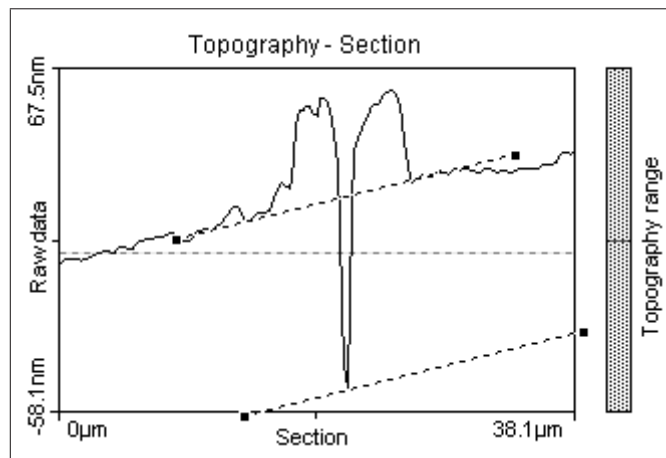


Figure 4.21: A cross section through the scan, showing how the depth of the line scratched into the PEDOT was measured.

The method of AFM scratching proved to be the most reliable, ensuring a thickness of 30 nm for the PEDOT layer was obtained after spinning the sample at 5000 rpm, for 35 sec after dripping the liquid onto the sample. It has to be said that there are too many variables, such as sample and temperature and consistency of the spinning speed, to achieve the same accuracy in thickness (i.e < 5 nm) as what was achieved with the QCM sensors.

4.5 Gold Sputtering

Using sputtering instead of thermal evaporation has certain pros and cons. One of the benefits is that the particles in the material layer has better adhesive properties [20]. Gold sputtering is used for this reason and is discussed in Chapter 5. To create a gold layer using sputtering, an Edwards Sputter Coater S150B was used. Vacuum is set to 2×10^{-2} mbar, before the argon inlet is opened. Deposition is started by switching on the high voltage when the vacuum reaches 4×10^{-1} mbar. The thickness of deposition is controlled by setting the time of deposition and the ion current. It was calibrated using polished silicon samples with Rubylith masks applied and measuring the thickness with the AFM. A 5 minute deposition time, with an ion current of 32 mA, produced a 40 nm layer of gold.

4.6 CuPc nanowires

To see if the CuPc would form nanowires or nanofibers on ITO glass, four samples were prepared, using the sputtering technique described above, to make ITO samples with 40 nm of gold on. The samples were then used with mask 2, and the sample heater in the thermal evaporator, to heat the different samples to the different temperatures while depositing a 15 nm (the same thickness the layer will be in the device) layer of CuPc.

After scanning all four samples with the AFM, there was no evidence of nanowires forming. This could be attributed to two main factors. Firstly, that the crystalline matching of a gold layer on silicon is much better than on ITO glass. The second factor could be the CuPc thickness. There is no point in increasing the CuPc layer, because any advantage of nanofibers would be cancelled out by the fault in diffusion length. However, 15 nm did not prove thick enough for nanowires to start forming ([2] reported nanowires with diameters ranging between 16 nm and 50 nm).

There was, however, an improvement in surface roughness. The measured surface roughness values at the different temperatures are shown in Table 4.3. The improvement in surface roughness of the CuPc, even though it was deposited on gold, is in concurrence with other work [30], where surface roughness measurements were done after both the CuPc and C₆₀ layers were deposited. Chiu *et al* [30] showed that an increase in substrate temperature during deposition improved the surface roughness of their devices, as well as a slight increase of device efficiency.

Table 4.3: Different surface roughness results for CuPc films, deposited at different temperatures on gold covered ITO glass. Surface roughness was measured with a contact tip, over a 3 μm^2 area on the AFM.

Substrate Temperature	Gold thickness	CuPc thickness	CuPc surface roughness
room temperature	40 nm	15 nm	36.98 nm
100 °C	40 nm	15 nm	25.95 nm
150 °C	40 nm	15 nm	19 nm
200 °C	40 nm	15 nm	11.03 nm

4.7 Conclusion

At this point, a description of the deposition techniques used for all the materials needed to construct thin film organic solar cells have been given. The calibration for each material was done to ensure the repeatability of each material deposition to the correct thickness. Chapter 5 will describe the different variations of solar cells built, and how they were tested.

Chapter 5

Testing

This section describes AM1.5G conditions for solar cell testing. It also describes how manufactured solar cells were tested and compared for optimal inhouse operation, before AM1.5G conditions could be achieved.

5.1 Making Contact

The first step in testing the built solar cells, is to make electrical contact to the anode and cathode, in order to extract current. In the laboratory, where a lot of superconducting work is performed, most people opt for using wire-bonding. Wire-bonding failed because of the thin layers used for the metal contacts. It was still viable to try and bond to the silver or directly to the ITO of Figure 3.3, but impossible to do on the thin aluminium layer. The pressure of the wire-bonding needle forces it straight through into the soft underlying organic layers, while the heat also distorts the films.

A simple two contact PCB was designed to fit underneath the silver and aluminium. Silver conducting paint was used to fix the solar cell to the PCB. Care had to be taken to ensure that the silver paint did not flow and connect to the wrong layer, as they are only millimetres apart. Some success was achieved in using masking tape to block the paint. Another challenge was using the correct quantity of paint. Using too much paint deformed the layer, as seen in Figure 5.1, rendering the device useless. Thinning the paint with acetone made the paint dry too quickly, prohibiting the solar cell from connecting to the PCB, and falling off. Using a little more made the acetone penetrate the aluminium before evaporating and destroy the device, as shown in Figure 5.2.

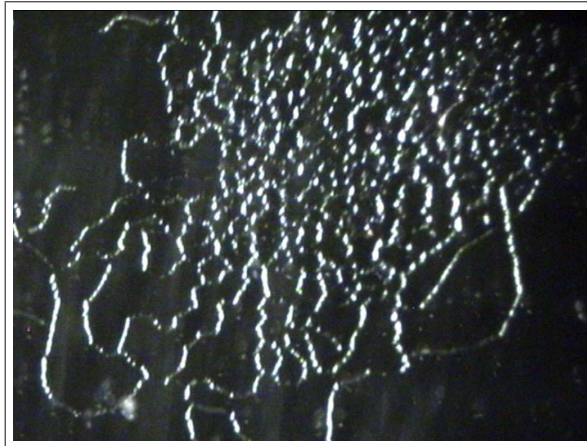


Figure 5.1: The deformation in the layers of the solar cell, made by placing the sample on wet conductive paint.

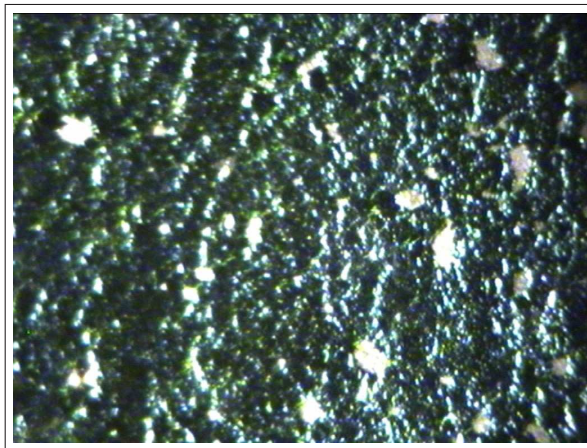


Figure 5.2: The deformation in the layers cause by acetone used to thin the conductive paint.

It soon became clear that, even if the correct quantity of paint was found, the paint eventually cracked the layers when it dried between the PCB and the glass, as can be seen in Figure 5.3.



Figure 5.3: Cracks shown under optical microscope caused by the conductive paint crimping between the sample and PCB when it dries.

Moving away from the conductive paint, a press contact was tried. Small beryllium copper springs were made and soldered to the PCB. The solar cells were then pressed down on to the springs. Pressing down evenly became a big problem, and any movement in the solar cell damaged the aluminium film. To try something softer to press on, a conductive copper tape was obtained from RS Components, which also had a conductive glue. This too, proved unsuccessful. When sticking the tape on the PCB, and pressing down on it with the solar cell, the layers were damaged on the edges of the tape. Sticking the tape on the aluminium layer on the solar cell itself, also did not work as the glue on the tape is too strong, which caused it to tear through the solar cell's layers, as shown in Figure 5.4, with any movement or bend in the tape (as a result of the roll it came on).

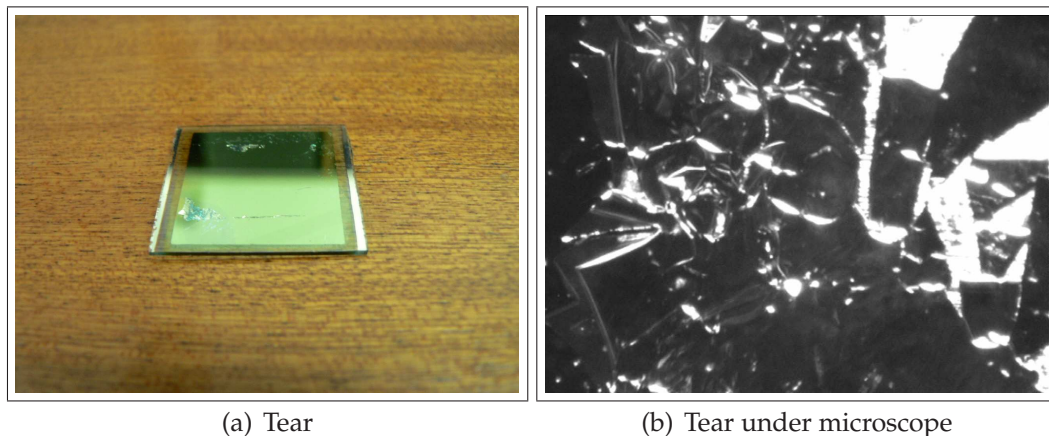


Figure 5.4: The glue on the copper tape deforming the layers. The damage looks like a tear in the films (a) and like crinkled layers under a optical microscope (b).

Finally it seemed that no method at all, proved the best solution. The solar cells were simply placed, very gently, on the PCB, and held in place with two screw in blocks over the silver strips, as shown in Figure 5.5. This was obtained by glueing the PCB onto a plate of Perspex, and cutting thread in the Perspex. The PCB was also polished with an abrasive stone, ethanol and a metal polish.

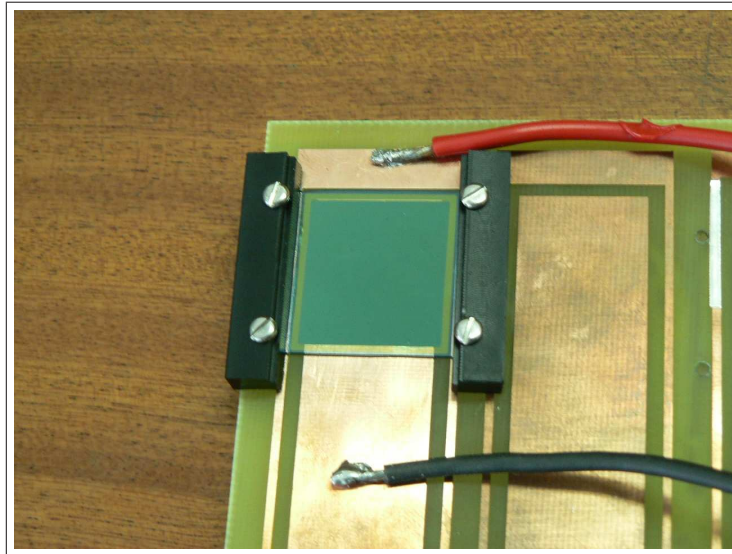


Figure 5.5: Screw connectors over the silver strips clamping the solar cell onto a PCB.

5.2 AM1.5G

In literature, the preferred standard spectrum of irradiance for solar cell testing is referred to as AM1.5G. This denotes the position of the sun at a 48 deg angle to the zenith, with a total intensity of 100 mW/cm^2 at a temperature of 25°C .

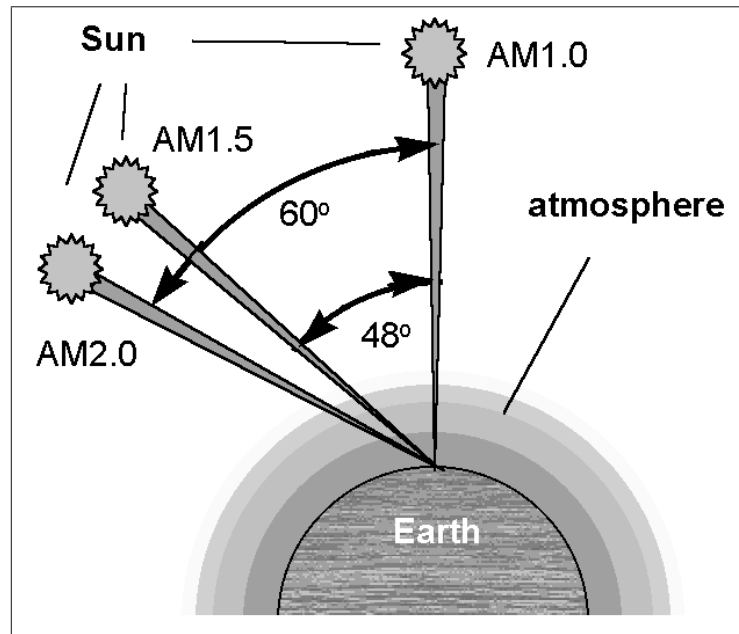


Figure 5.6: The change in Zenith angle increases the path length of solar radiation, as measured in Air Mass [31].

The power conversion efficiency (η) of a photovoltaic cell is dependent on three parameters, short circuit current, open circuit voltage and fill factor. The fill factor (FF) of a solar cell under AM1.5 illumination is obtained by a current-voltage characterisation and is the measure of the diode behaviour of the photovoltaic device. The FF is given by Equation (5.1). The open circuit voltage is independent of the cell area [32], and the efficiency is then defined as the power produced by the cell at the maximum power point under standard test conditions, divided by the power of the incident radiant flux [33] given by Equation (5.2). The use of this standard irradiance value is particularly convenient, since the cell efficiency in percent is then numerically equal to the power output from the cell in mW/cm^2 [33].

$$\begin{aligned} FF &= \frac{P_{max}}{V_{oc} \cdot I_{sc}} \\ &= \frac{V_{max} \cdot I_{max}}{V_{oc} \cdot I_{sc}} \end{aligned} \quad (5.1)$$

$$\begin{aligned} \eta &= \frac{P_{max}}{P_{in}} \\ &= I_{sc} \cdot V_{oc} \frac{FF}{P_{in}} \end{aligned} \quad (5.2)$$

As the University of Stellenbosch does not have facilities to do AM 1.5G testing, an arrangement was made with the University of Cape Town (UCT) to use their facilities. However, before going to UCT to do the final testing, a simple inhouse method was required to compare devices. Of course normal sunlight would do, but as the sun does not shine every day, and certainly not with the same intensity, a light box was built. Figure 5.7 shows the box, $1\text{ m} \times 0.6\text{ m} \times 0.6\text{ m}$, completely lined on the inside with aluminium foil to reflect light inwards. Light was provided from a 400 Watt Phillips daylight bulb. To insulate the solar cell, placed at the bottom, from heat generated by the bulb, two sheets of 3 mm glass was placed in the middle. Furthermore, two 120 Volt fans were connected in series over the bulb, one pushing in cold air into the box, the other removing the hot air. The cells were connected to a series of resistors (between $1\ \Omega$ and $100\ \text{k}\Omega$) to measure the IV curves.



Figure 5.7: Lightbox used for solar cell testing. The box is covered with aluminium foil for reflection inside. The 400 W bulb is cooled by two 120 V fans, and two sheets of glass insulates the samples from heat generated by the light.

To measure the light intensity inside the box, a Kipp & Zonen SP Lite pyranometer was obtained from the Department of Mechanical and Mechatronic Engineering. The pyranometer was placed on the bottom of the box, where the solar

cell would be placed when tested. The reading on the pyranometer was 39 mV, which relates to 53 W/m^2 , which is the intensity at which all the manufactured solar cells were tested in the light box. To calculate the intensity, Equation (5.3) was used, where E_{solar} is the irradiance in Watt per square meter, U_{emf} is the output voltage in micro volts, and S the sensitivity of the pyranometer given as $76 \mu\text{V/Wm}^{-2}$.

$$E_{solar} = \frac{U_{emf}}{S} \quad (5.3)$$

5.2.1 Testing the First design

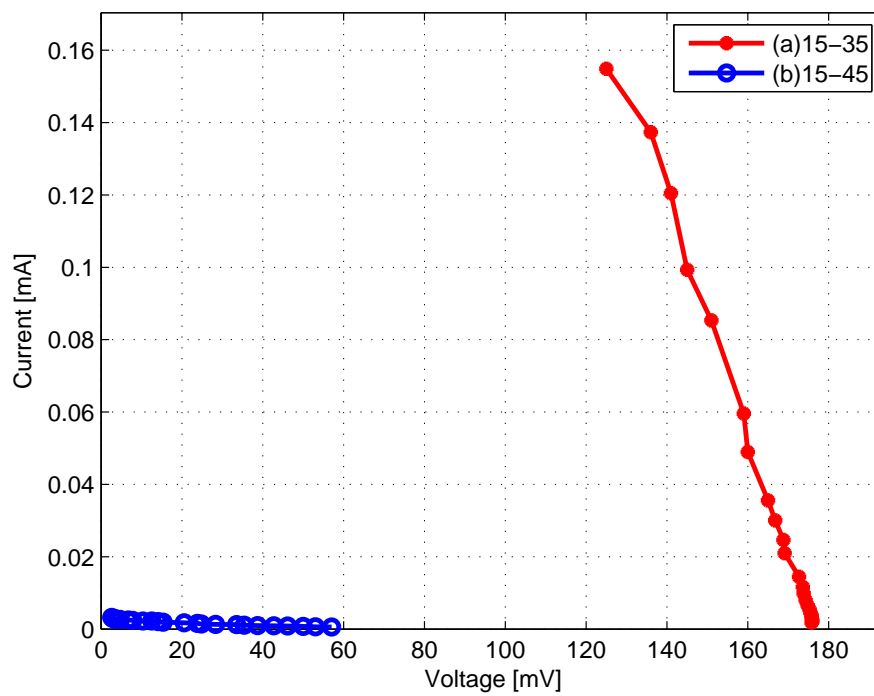
When testing the first design made in Chapter 3.2.1, a short circuit was measured over the cell. Since the cells are measured by making contact to the silver and aluminium contacts, a short circuit can occur in one of two ways. Firstly, the aluminium could be touching the ITO. Secondly, the probe used could be pushing straight through all the layers to the ITO. In this case, the first reason was the problem, with the aluminium layer overlapping the other layers. The design was changed by adding more masks to the manufacturing process, to avoid overlapping.

5.2.2 Test results from the pyramid design

The first working solar cell tested was the one designed in Chapter 3.2.2. Once a working device could be placed on the test PCB an open circuit voltage could be measured. Several variations in the organic semiconductor layer thicknesses needed to be implemented to estimate the correct exciton diffusion lengths. Table 5.1 summarises the different variations on layer thicknesses used.

Table 5.1: Different layer thicknesses of organic semiconductors and results obtained.

CuPc	C ₆₀	Results
15 nm	40 nm	no result
10 nm	40 nm	no result
20 nm	40 nm	Figure 5.9
15 nm	35 nm	Figure 5.8 (a)
15 nm	45 nm	Figure 5.8 (b)

**Figure 5.8:** Current versus voltage plot for a device layout of (a) ITO/CuPc 15nm/C₆₀ 35nm/Al 100nm (b) ITO/CuPc 15nm/C₆₀ 45nm/Al 100nm.

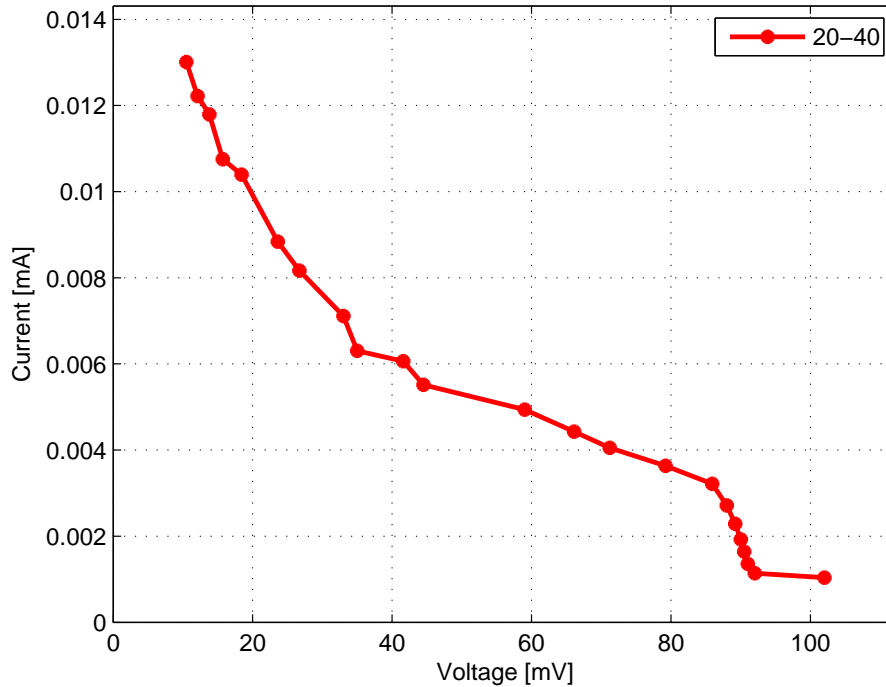


Figure 5.9: Current versus voltage plot for a device layout of ITO/CuPc 20nm/C₆₀ 40nm/Al 100nm.

5.2.3 Adding EBL

As can be seen in Table 5.1, results were not obtained in all the different structures. After several iterations of building the five structures in Table 5.1, the main reason for devices not working was established as the aluminium layer penetration during deposition. Aluminium's evaporation temperature is very high in comparison to the organic materials. This leads to the aluminium penetrating the C₆₀ layer. Penetration through the C₆₀ layer results in two measurable malfunctions in the devices. Firstly, a short circuit, where the aluminium penetrates straight through to the ITO as described above. Secondly, and more commonly, the aluminium penetrates through and connects to the CuPc. This means that the CuPc is touching both contacts, and a Schottky junction type cell has been built instead. The difference is clearly measurable in such a cell with Al penetration, giving either a short circuit, i.e. no output voltage, or a Schottky junction, giving a very low output voltage. Typically a low output voltage is in the range of 1 mV to 25 mV, without being able to deliver current to the resistors used to plot the IV curves.

Solving the aluminium penetration was done in two parts. Firstly the design was changed to that of Chapter 3.2.3, adding BCP as an exciton blocking layer. Secondly the deposition rate of the aluminium was kept very low (under one Angstrom per second). Keeping the deposition rate low, however, proved to be difficult with the tungsten boats. The aluminium tends to flow around the boat when it starts melting, dripping out of the boat and shortening the tungsten boat lifetime due to its difference in thermal expansion to that of tungsten. Instead tungsten wires were used, wrapping the aluminium foil around the wire. A lower deposition rate was obtained by rapidly heating the wire until wetting (wetting is the term used to describe the aluminium melting and covering the whole wire) occurred, and then turning down the current before opening the shutter of the thermal evaporator. To do a 100 nm or 150 nm layer of aluminium at such a slow deposition rates, takes very long. Another benefit of using the wire deposition, is that more than one wire can be used. This meant that by using two wires, the deposition rate could be doubled, without increasing the aluminium temperature, cutting the deposition time in half.

BCP was added as an exciton blocking layer to the five structures mentioned in Table 5.1, and several iteration were built again. Results were obtained as shown in Table 5.2. As can be seen in Table 5.2, still only a few results could be obtained.

Table 5.2: Different layer thicknesses of organic semiconductors, with BCP, and results obtained.

CuPc	C₆₀	BCP	Results
15 nm	40 nm	10 nm	Figure 5.10(a)
10 nm	40 nm	10 nm	Figure 5.10(b)
20 nm	40 nm	10 nm	no result
15 nm	35 nm	10 nm	no result
15 nm	45 nm	10 nm	no result

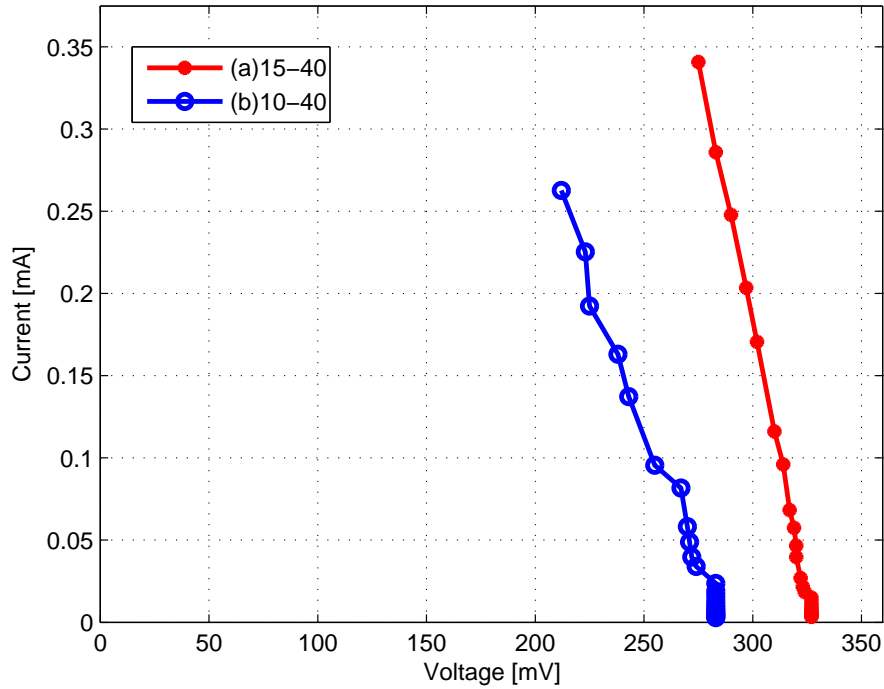


Figure 5.10: Current versus voltage plot for a device layout of (a) ITO/CuPc 15nm/C₆₀ 40nm/BCP 10nm/Al 100nm (b) ITO/CuPc 10nm/C₆₀ 40nm/BCP 10nm/Al 100nm.

However, with the results obtained thus far, two interesting conclusions can be drawn. Firstly, even though the measured structure with the 15 nm CuPc and 40 nm C₆₀ had a BCP layer added, it can still be assumed that 15 nm and 40 nm are the correct exciton diffusion lengths respectively. This assumption is based on the order of magnitude in improvement in comparison with the other structures, as can be seen in Figure 5.11 when all the results obtained so far are plotted on the same graph. The second conclusion, if taking the first into account, is that cells with a layer thicknesses smaller than the exciton diffusion length, perform better than cells with layers thicker than L_D . This means that losses associated with absorbed excitons not reaching an interface to be separated are greater than losses associated with unabsorbed photons.

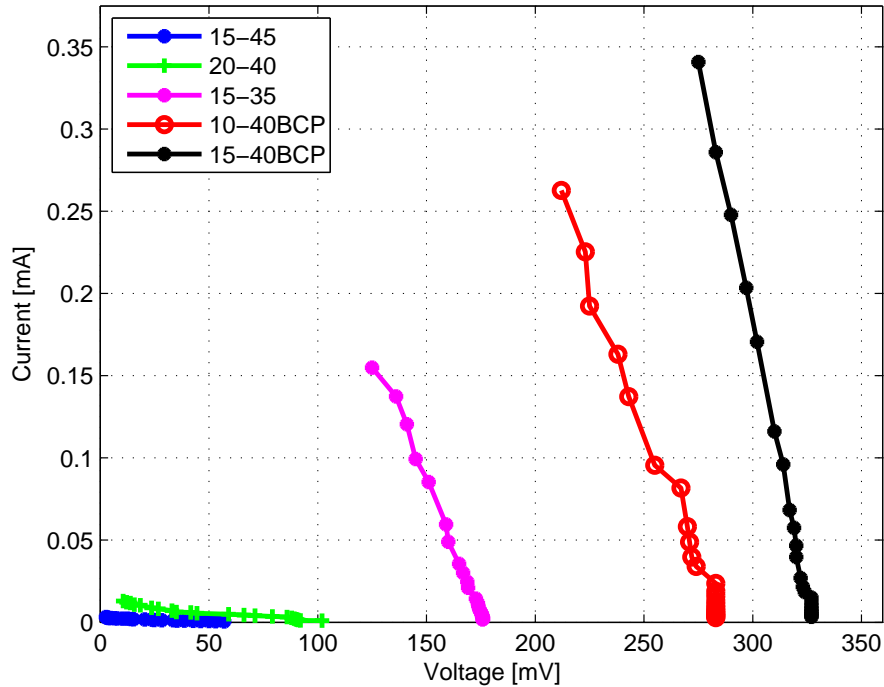


Figure 5.11: IV curves of all the variations in semiconductor thickness, although two include BCP. The correct exciton diffusion length can still be read off this graph.

To address why so few results could be obtained, two additions were made. Firstly, to overcome the cells that still made short circuits, the structural integrity was addressed. Since adding the BCP layer, the thickness of the aluminium was deposited as 100nm, instead off 150nm, to further help prevent penetrating aluminium. This means that the cells are even more susceptible to damage. If the cell moves while it is being placed on the PCB, or if it is tightened too much, even a little bit, the aluminium scratches and the device produces a short circuit. To overcome this, gold was sputtered onto the aluminium. It was reported by [20], that materials that are sputtered, have a far superior intermolecular binding strength to those being thermally evaporated. This held true for the solar cells built. As can be seen in Figure 5.12, the silver tape with conducting glue tried before, could now be stuck onto the gold surface, without damaging the underlying films. This now meant that the cells are more rugged, and could be placed on and removed from the PCB without damage. The second addition made is described in Section 5.2.4.

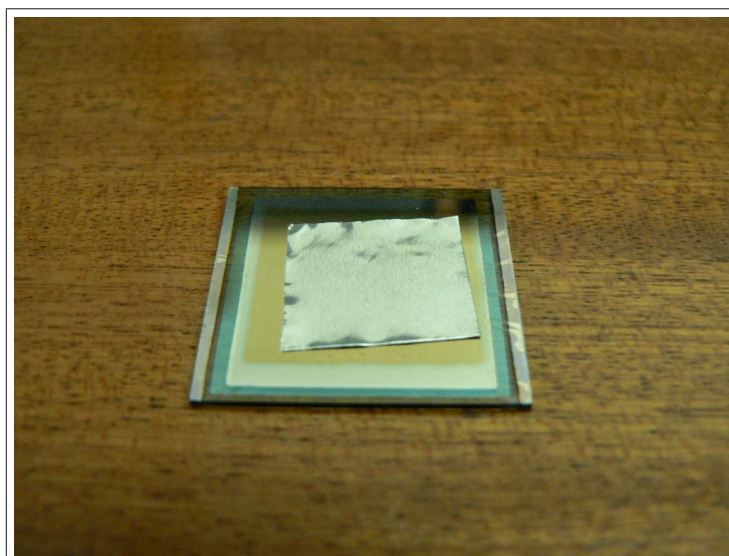


Figure 5.12: Completed solar cell as seen from the back. The conductive tape placed over a sputtered gold layer can be seen. The tape makes handling and testing of the cell more rugged.

5.2.4 Adding PEDOT:PSS

Several cells were again constructed, this time with only the 15/40 structure in the semiconductor layers, as it is now assumed to be the correct thicknesses, but adding BCP, gold, the conductive tape and PEDOT:PSS as the front exciton blocking layer as described in Chapter 3.2.4. The PEDOT serves two roles, firstly as an exciton blocking layer as described in Chapter 3.2.4, and secondly as a mechanical smoothing layer. Since the ITO glass has a surface roughness of around 40 nm, it is clear that deposition of a 15 nm layer of CuPc might leave peaks of the ITO sticking out. This means that when the C_{60} is deposited, it connects to the ITO, and later the aluminium. So once again a Schottky junction is created instead of the heterojunction, causing lower than expected output results.

However, at first, adding the PEDOT and gold layer, no results could be obtained. All the devices still made short circuits. Two new problems were found, firstly, by observing the cells under a microscope. As can be seen in Figure 5.13, micron sized cracks have formed on the cells. These cracks are visible from both sides of the cells, and are attributed to moisture. As reported by [18], it is a disadvantage of BCP thin films, which tend to crystallise in the presence of moisture. This can be corrected by doping the BCP with 5% to 15% of PTCBI by means of co-evaporation. Unfortunately the available thermal evaporator has only one source, and co-evaporation is thus not possible.

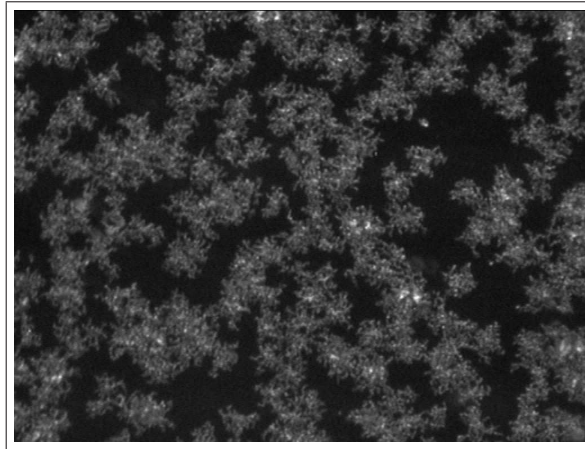


Figure 5.13: Micron sized cracks in solar cell. These cracks are visible under a optical microscope, and can be seen on both sides of the solar cell. They are caused by the BCP layer reacting to moisture.

The second problem, unfortunately, was the gold sputtering. Even though it protected the cells from scratching, it deposited through to the ITO. It was found that the gold penetrated by building several devices, selectively removing all suspect layers, as for instance BCP, and adding gold to half of the test group. Test result were conclusive in that none of the samples with gold produced anything but a short circuit. This can probably be attributed to dust or small particles landing on the samples. If the samples are inspected from the back, small dots of light can be seen, indicating an aluminium layer that is not 100% uniform. It is difficult to prove conclusively that dust is the only problem, since removal of such particles is impossible, because the laminar flow chamber for the thermal evaporator is no longer operational.

The gold and tape layers were subsequently taken out of the equation, and a new batch of BCP was used. The new BCP was used more carefully, in that it was heated under vacuum for longer, before deposition, to ensure that no moisture could be transferred to the sample. After inspection under the microscope revealed no cracks, the first full structure i.e. including the PEDOT was tested, going back to the careful placement on the blank PCB. The result, as shown in Figure 5.14(a), shows an IV curve smaller than expected. Adding the second exciton blocking layer, a resulting IV curve bigger than previous results of the 15/40 structure were expected.

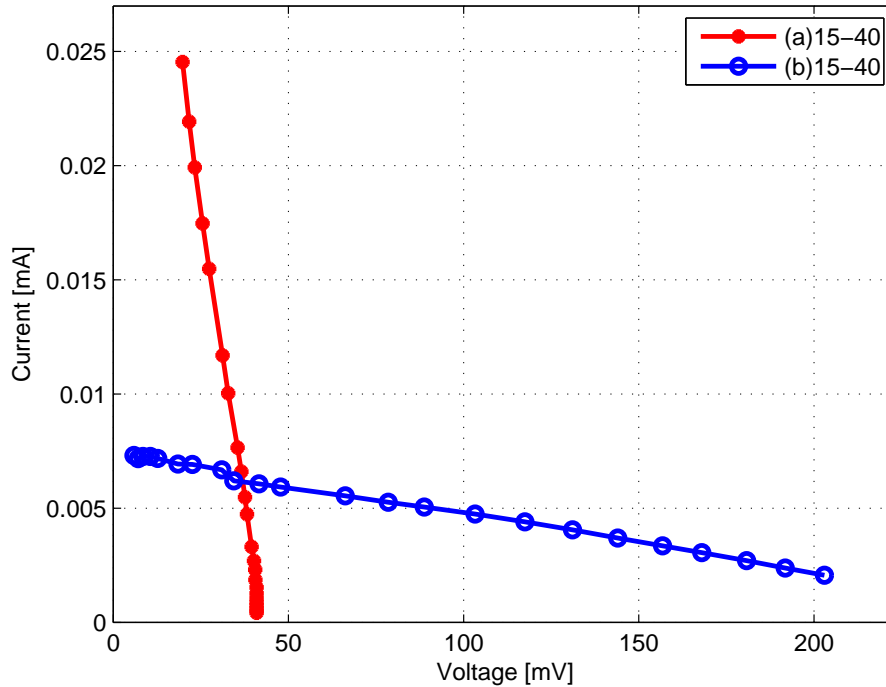


Figure 5.14: IV curve of two complete cells, including PEDOT, (a) before and (b) after QCM recalibration.

The problem was the calibration of the QCM sensors. After repeated experiments to solve the contact problem, too much lifetime was lost on the sensors. After recalibration of the organic material's QCM sensors, Figure 5.14(b) was obtained. As can be seen from the graph, a definite improvement on the output voltage can be seen, although the current at lower voltages has dropped. This is an indication that the series resistance is too high, something that could be attributed to the BCP layer being too thick. It thus necessitated recalibrating the other QCM sensors for BCP and the contact metals, before building a device for AM1.5G testing.

5.2.5 AM1.5G Results

A new batch of four samples, with the same structure of PEDOT 30nm/CuPc 15nm/C₆₀ 40nm/BCP 10nm/Al 100nm, was made and taken to UCT along with the sample shown in Figure 5.14 and a sample without BCP. Even though five out of the six are supposed to be the same, they were all taken to UCT to be tested, to make provision for damage that can occur during setup. The other sample was taken to see the effect of removing an exciton blocking layer, i.e. to see if it does improve performance.

All the cells were tested with UCT's SPI-cell tester, at AM 1.5G equivalent (100 mW/cm^2) conditions. Sample temperatures were kept between 25°C and 26°C . The first positive result from a manufacturing point of view, is that all the samples worked, and could provide results. The second positive result is shown in Figure 5.15, which shows the IV curves of the four new samples, made as described above. As can be seen, the maximum current for all four are grouped close together. There is, however, a slight deviation in the open circuit voltage values. This is not too unexpected, as it was mentioned in Chapter 4.4.2, the devices will not be 100% the same, because of the difficulty in reproducing the thickness of the PEDOT layer. The PEDOT layer thickness will vary with the temperature of its deposition, and the consistency of the vacuum chuck's spinning speed. Thus the resistance of every cell will be different, as the resistance will change with the layer thickness.

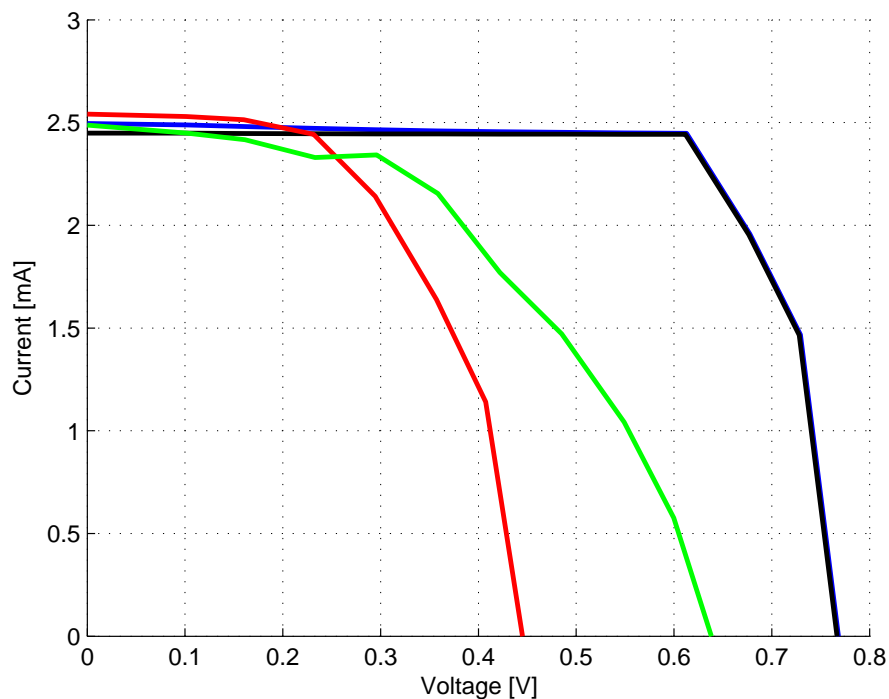


Figure 5.15: IV curve of four different samples under AM1.5G 100 mW/cm^2 , all manufactured in the same way, with a structure PEDOT 30nm/CuPc 15nm/ C_{60} 40nm/BCP 10nm/Al 100nm. The four plots indicate that a manufacturing process is not 100% reliable.

Another interesting result to note is that the resistance of the cells change with exposure to light. It is as if the cell cures when exposed to light, and the resistance and in fact the performance changes. This can be seen in Figure 5.16, showing the

same cell's IV curves as measured with the SPI-cell tester. After each time the cell was exposed to the light, and its IV curve measured, the resistance was measured separately. The cell's resistance dropped from 140 k Ω to 88 k Ω from after the first to the last test.

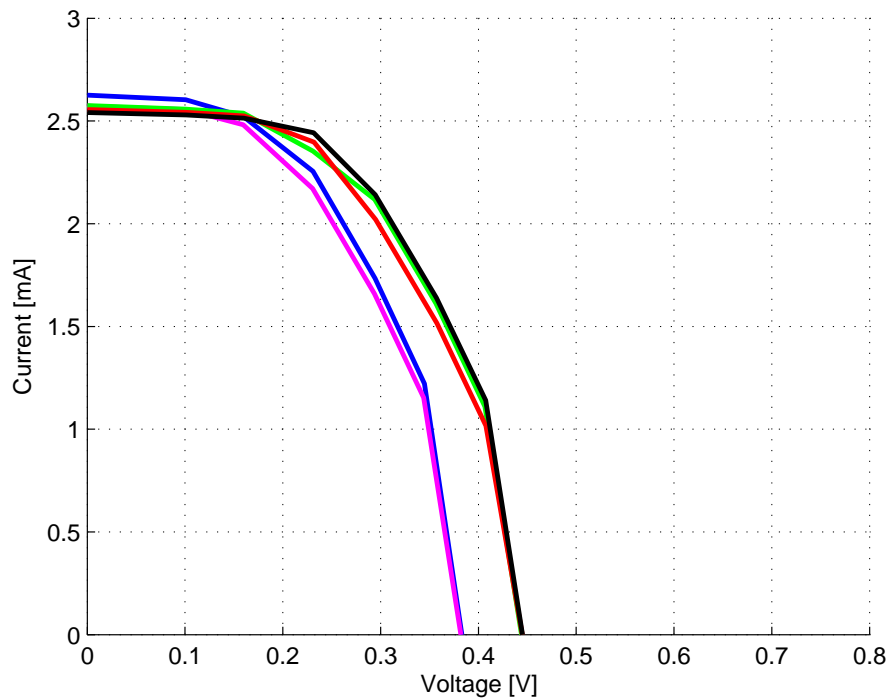


Figure 5.16: One of the cells with a structure PEDOT 30nm/CuPc 15nm/C₆₀ 40nm/BCP 10nm/Al 100nm tested under AM1.5G, showing the variation in cell resistance with repeated exposure.

In the last comparison, the influence on performance from the BCP layer can be seen. Figure 5.17 (b) shows the IV curve of the cell from Figure 5.14 (b), as tested with the SPI-cell tester, along with the cell without a BCP layer, Figure 5.17 (a). This figure confirms that a BCP layer, as an exciton blocking layer, does improve the device performance.

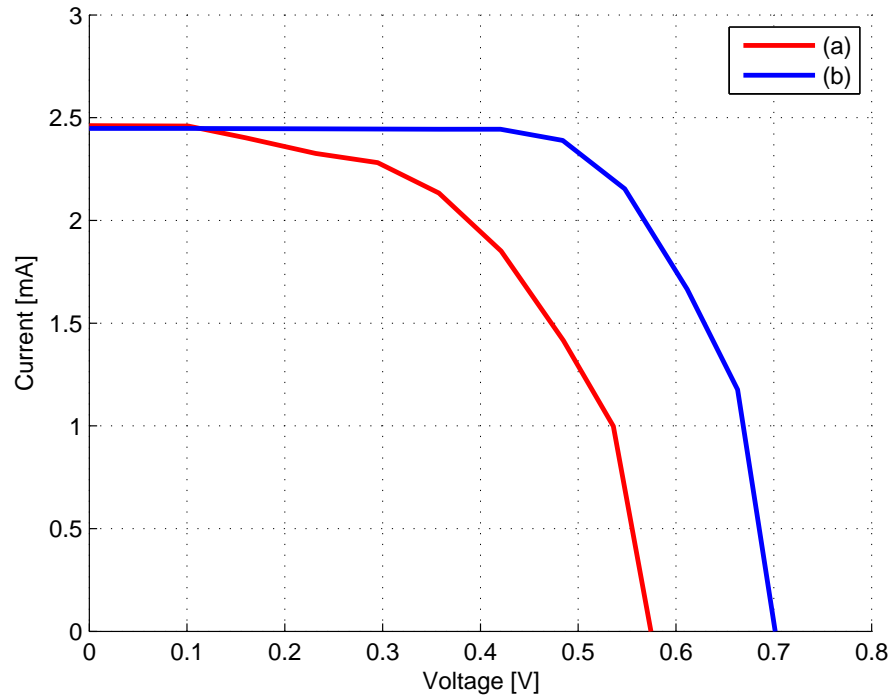


Figure 5.17: IV curve of cells with and without the BCP layer. The cells have structures (a) PEDOT 30nm/CuPc 15nm/C₆₀ 40nm/Al 170nm and (b) PEDOT 30nm/CuPc 15nm/C₆₀ 40nm/BCP 10nm/Al 100nm. This shows the importance of the second exciton blocking layer.

5.3 Conclusion

Several cells with the 15/40 structure (glass/ITO 160nm/PEDOT 30nm/CuPc 15nm/C₆₀ 40nm/BCP 10nm/Al 100nm) were taken to UCT to test with their SPI-cell tester. Due to various possible discrepancies in manufacturing, especially the unstable thickness of the spun on PEDOT layer, the values obtained for efficiency vary. Table 5.3 summarises the range of results obtained.

Table 5.3: Summary of experimental results under AM1.5 conditions for solar cell with structure: glass/ITO 160nm/PEDOT 30nm/CuPc 15nm/C₆₀ 40nm/BCP 10nm/Al 100nm.

V_{oc}	0.382 V - 0.768 V
I_{sc}	2.458 mA - 2.637 mA
R_{series}	26.402 Ω - 66.844 Ω
R_{shunt}	1147.04 Ω - 13 206.3 Ω
FF	0.203 - 0.965
Efficiency	1.308 % - 4.959 %

It is interesting to note that the maximum current obtained at UCT, is more than twice the amount measured in the light box. There are two explanations for these results. Firstly, the SPI-cell tester used at UCT has double the light intensity (100 mW/cm² instead of 53 mW/cm²). The second reason is that the SPI-cell tester simulates sunlight. The light box, which uses a commercial light, often used in large industrial buildings, has a UV filter around it, to protect human eyes in the work place. Thus a large part of the light spectrum, in the lower wavelength range, is lost in the light box, where organic photovoltaic cells are more efficient. This can be seen in the absorption diagram for CuPc shown in Figure 5.18. The range of wavelengths in Figure 5.18 is between 200 nm and 1000 nm. The reason therefore, is that the light at wavelengths beneath 300 nm is strongly absorbed by the glass, and above 900 nm is outside the range of most photovoltaic materials. This is also the reason why only the wavelengths of between 300 nm and 900 nm are considered in Chapter 6 for the simulations.

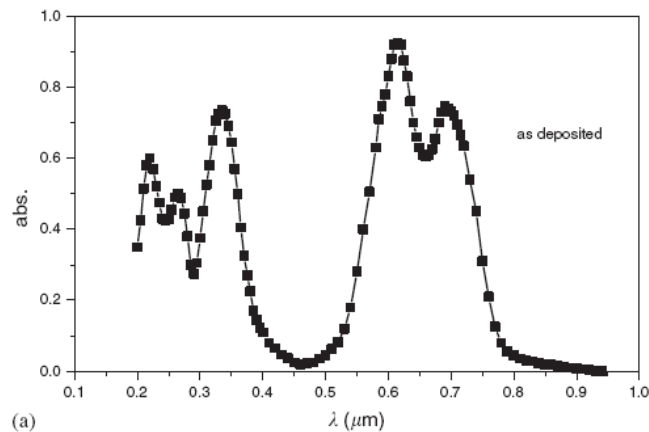


Figure 5.18: Absorption of CuPc at various wavelengths [34].

Chapter 6

Simulation

6.1 Commercial Software

One of the leading software packages used to model the working of solar cells, known as PC1D, was developed at the University of New South Wales. PC1D is now an open source package, and works with a graphical interface where the user can construct a device, and compile parameters on the device. PC1D has existing material parameter files for materials such as Si and GaAs, and comes with a one sun equivalent excitation file.

However, PC1D is not used to design organic solar cells, since organic solar cells are made of different materials, that do not require doping and are excited differently from inorganic solar cells. Instead, commercial software such as Silvaco could be used. Silvaco has a new application called "Organic Solar" [35]. Organic Solar is built into the existing ATLAS framework, and allows the steady-state, transient and AC simulation of both the electrical and optical behaviour of organic photovoltaic cells. Some of the capabilities include the simulation of:

- Transfer Matrix Method
- Exciton generation and recombination rates
- Exciton densities
- Exciton diffusion
- Dissociation characteristics

Commercial packages such as Silvaco unfortunately come with very expensive licenses. Therefore, a simulation was done using an equivalent circuit model

together with the Transfer Matrix Method, in a linear algebra package, Matlab, from Mathworks. All the equations solved in the TMM were implemented as functions in Matlab, and can be seen in Appendix C.

6.2 Equivalent Circuit Model

The general equivalent model for solar cells is the diode circuit shown in Figure 6.1 (a), because of the similarity to a p/n junction. The real model, including series and shunt resistors, is shown in Figure 6.1 (b).

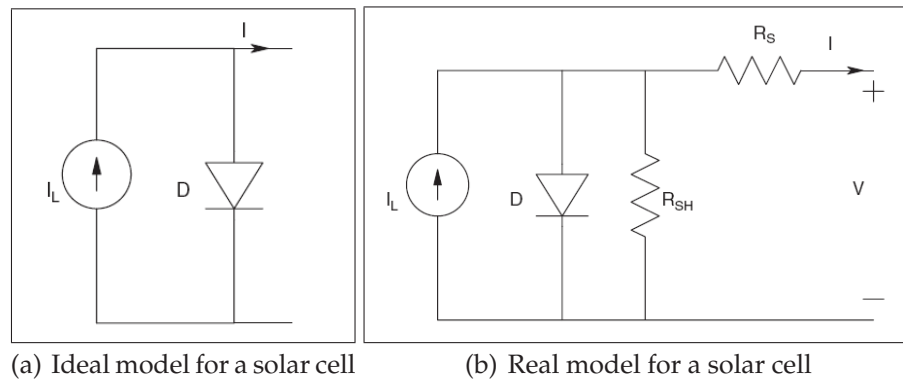


Figure 6.1: Equivalent circuit model for photovoltaic cells

The model shown above was improved by [3], as shown in Figure 6.2, without parasitic series and shunt resistors. This model can be used to better describe the behaviour of organic photovoltaic devices, when the assumption is not made that the photo generated current is constant from short circuit to open circuit conditions. This would prove to be more valid in general. The model used in this work, as illustrated in Figure 6.3, was described by [4]. The current is given by Equation 6.1, as a function of photo generated current (I_{ph}). The photo generated current is calculated as a function of absorption, using the transfer matrix method (TMM) to account for optical interference, shown in Section 6.3.

$$I' = I_{ph} - I_s \left[\exp\left(\frac{qV_j}{kT}\right) - 1 \right] - \frac{V_j}{r_p} \quad (6.1)$$

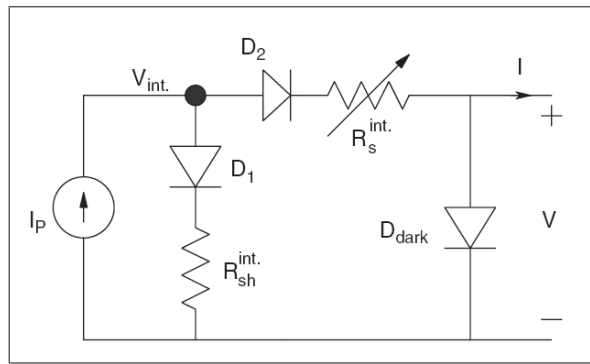


Figure 6.2: Equivalent circuit model as proposed by [3].

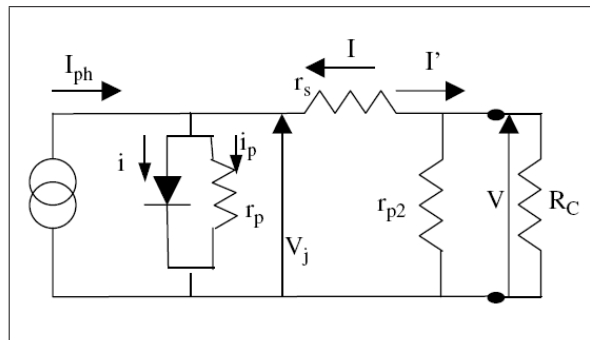


Figure 6.3: Equivalent circuit model as proposed by [4], used in this work.

6.3 Optical Interference Method

In the optical interference method, as described by [18] and [36], the incident light is modelled as a wave, as is done in electromagnetic applications, to propagate through the device. This light is assumed to fall perpendicular on the solar cell, which is assumed to be a stack of semi-infinite layers, as illustrated in Figure 6.4. Each layer represents a different material in the solar cell's structure. Thus, each layer has a thickness, d_j , and complex index of refraction,

$$\bar{n}_j = n_j + ik_j. \quad (6.2)$$

The refractive indices for all the layers are wavelength dependant, and the values used in this simulation are given in Appendix B.

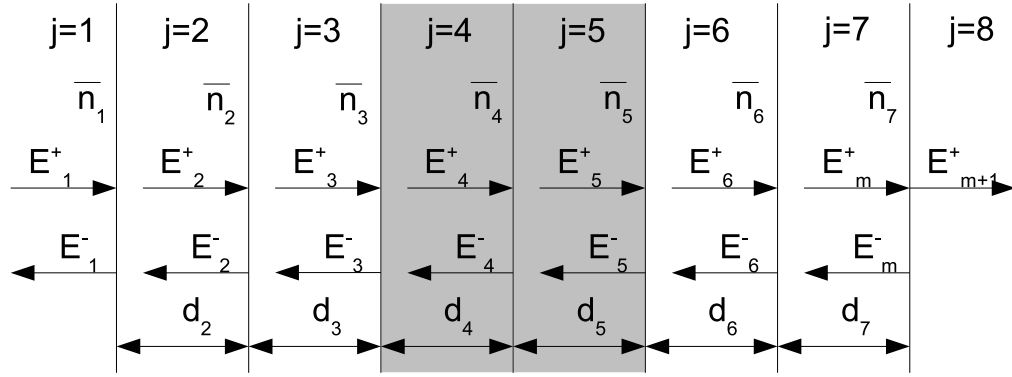


Figure 6.4: Geometry of the semi infinite layer stack used to model light propagation. The light propagation is modelled as an electromagnetic wave, entering on the transparent substrate side ($j = 1$). No light enters from the air ($j = 8$) at the back electrode.

As the optical field propagates through the layers, there will be transmission and reflection at every interface between two layers j and k ($k = j+1$). The behaviour at the interface is described by

$$\begin{bmatrix} E_j^+ \\ E_j^- \end{bmatrix} = I_{jk} \begin{bmatrix} E_k^+ \\ E_k^- \end{bmatrix}, \quad (6.3)$$

where I_{jk} is a 2×2 matrix, called the interface matrix or matrix of refraction, as shown in Equation (6.4)

$$I_{jk} = \begin{bmatrix} \frac{1}{t_{jk}} & \frac{r_{jk}}{t_{jk}} \\ \frac{r_{jk}}{t_{jk}} & \frac{1}{t_{jk}} \end{bmatrix}. \quad (6.4)$$

In the above equations, E_j^\pm and E_k^\pm are components of the optical electric field propagating left and right as shown by Figure 6.4, for layers j and k , where t_{jk} and r_{jk} are Fresnel complex transmission and reflection coefficients given by

$$t_{jk} = \frac{2\bar{n}_j}{(\bar{n}_j + \bar{n}_k)}$$

and

$$r_{jk} = \frac{(\bar{n}_j - \bar{n}_k)}{(\bar{n}_j + \bar{n}_k)}.$$

Similarly, as the wave travels through a layer j , it experiences absorption and a phase change described by the layer matrix or phase matrix as

$$L_j = \begin{bmatrix} e^{-i\tilde{\zeta}_j d_j} & 0 \\ 0 & e^{i\tilde{\zeta}_j d_j} \end{bmatrix}, \quad (6.5)$$

where

$$\tilde{\zeta}_j = \left(\frac{2\pi}{\lambda}\right)\tilde{n}_j \quad (6.6)$$

and λ is the wavelength. The relationship between the two outermost layers, i.e. the glass substrate and air outside the aluminium, is given by

$$\begin{bmatrix} E_0^+ \\ E_0^- \end{bmatrix} = S \begin{bmatrix} E_{m+1}^+ \\ E_{m+1}^- \end{bmatrix}. \quad (6.7)$$

S is the transfer matrix, and is given by

$$S = \begin{bmatrix} S_{11} & S_{12} \\ S_{21} & S_{22} \end{bmatrix} = \left(\prod_{n=1}^m I_{(n-1)n} L_n \right) I_{m(m+1)}. \quad (6.8)$$

As we are interested to find the optical electric field for every layer, at any distance x into the layer, the system can be split into two partial transfer matrices given by the total multilayer transfer matrix

$$S = S_j^- L_j S_j^+.$$

The two partial subsystems are again defined as propagation of the field in the left

$$S_j^- = \left(\prod_{n=1}^{j-1} I_{(n-1)n} L_n \right) I_{(j-1)j}, \quad (6.9)$$

and right

$$S_j^+ = \left(\prod_{n=j+1}^m I_{(n-1)n} L_n \right) I_{m(m+1)}, \quad (6.10)$$

of the multilayer stack as indicated by Figure 6.4. The total internal electric field, as a result of the incident wave, at any position x , in any layer j , can be given as the sum of the propagation in the left and right directions by

$$\bar{E}_j(x) = E_j^+(x) + E_j^-(x). \quad (6.11)$$

With some algebraic manipulation, Equation (6.11) can be written as

$$\bar{E}_j = (t_j^+ e^{i\zeta_j x} + t_j^- e^{-i\zeta_j x}) E_0^+, \quad (6.12)$$

with

$$t_j^+ = \frac{\frac{1}{S_{j11}^-}}{1 + \frac{S_{j12}^- S_{j21}^+}{S_{j11}^+ S_{j11}^-} e^{i\zeta_j d_j}} \quad (6.13)$$

and

$$t_j^- = t_j^+ \frac{S_{j21}^+}{S_{j11}^+} e^{i2\zeta_j d_j} \quad (6.14)$$

in terms of the total transfer matrix, given above. Figures 6.5 and 6.6 shows the simulated normalised plots of several wavelengths propagating through the device with structure Glass/ITO 160 nm/PEDOT:PSS 30 nm/CuPc 15 nm/C60 40 nm/BCP 10 nm/Al 100 nm.

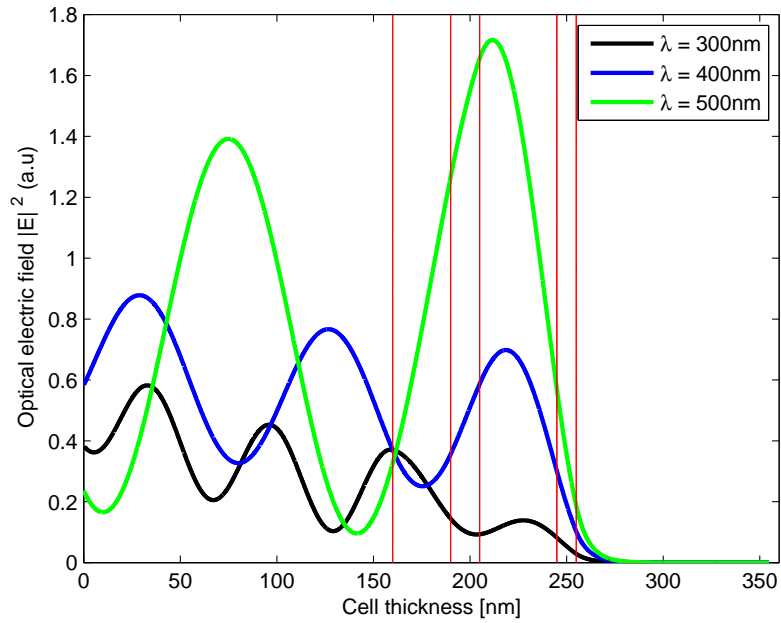


Figure 6.5: Simulated normalised plots of the optical electric field, at different wavelengths (as indicated), propagating through the device structure: Glass/ITO 160 nm/PEDOT:PSS 30 nm/CuPc 15 nm/C60 40 nm/BCP 10 nm/Al 100 nm.

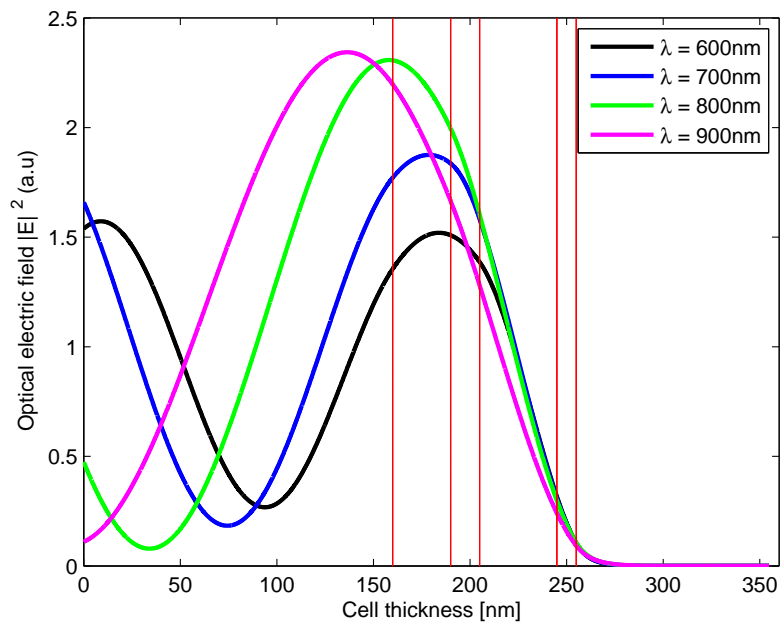


Figure 6.6: Simulated normalised plots of the optical electric field, at different wavelengths, propagating through the device structure: Glass/ITO 160 nm/PEDOT:PSS 30 nm/CuPc 15 nm/C60 40 nm/BCP 10 nm/Al 100 nm.

As was shown earlier with the manufacturing and testing of the solar cells, the PEDOT:PSS is the most challenging layer to produce in terms of accurate thicknesses. The test results also reflected this fact with the variation in cell series resistance. Another effect a change in layer thickness has, is on the impedance of the multilayer model, as seen by the incoming light wave. To illustrate this principle (the same principle of impedance matching is done to minimise reflection in anti-reflection coating in solar cell as well as electromagnetic technologies) Figure 6.7 shows the propagation of the optical electric field through similar devices, at the same wavelength, with only a variation in PEDOT thickness.

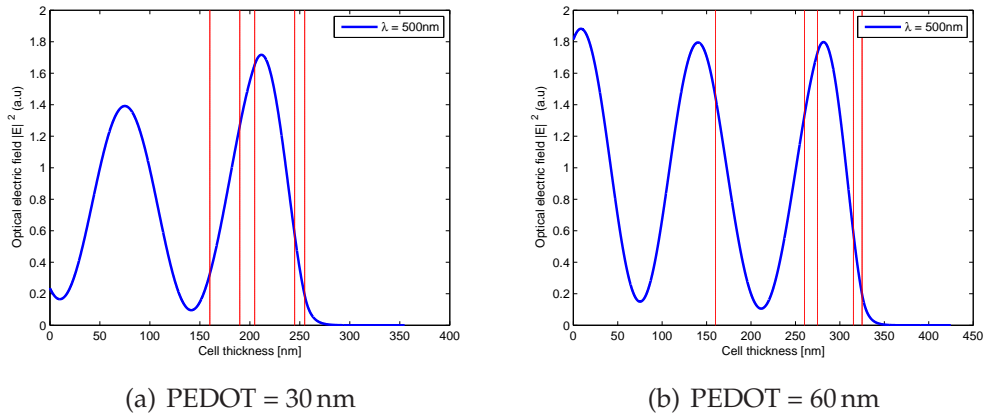


Figure 6.7: Simulated Optical Electric Field propagation, illustrating the effect of varying PEDOT thickness at a 500 nm wavelength of incident light on a device with a structure of Glass/ITO 160 nm/PEDOT:PSS x nm/CuPc 15 nm/C₆₀ 40 nm/BCP 10 nm/Al 100 nm.

Once the total electric field is known, the time averaged absorbed power can be calculated, as a function of position, as

$$Q(x) = \frac{4\pi c \epsilon_0 k_j n_j}{2\lambda} |E_j(x)|^2, \quad (6.15)$$

or corrected by [36] for the effect of the thick substrate layer as

$$Q_j(x) = \alpha_j T_j I_0 \left[e^{-\alpha_j x} + \rho_j^2 e^{-\alpha_j (2d_j - x)} + 2\rho_j e^{-\alpha_j d_j} \cos \left(\frac{4\pi n_j}{\lambda} (d_j - x) + \delta_j \right) \right] \quad (6.16)$$

In Equation (6.16), I_0 is the intensity of the incident light, α_j is the absorption coefficient given by

$$\alpha_j = \frac{4\pi k_j}{\lambda}, \quad (6.17)$$

T_j is the transmittance of the internal intensity

$$T_j = \left(\frac{n_j}{n_0}\right) |t_j^+|^2, \quad (6.18)$$

with ρ and δ given by

$$\rho_j = \sqrt{\left[\text{imag} \left(\frac{S_{j21}^+}{S_{j11}^+} \right) \right]^2 + \left[\text{real} \left(\frac{S_{j21}^+}{S_{j11}^+} \right) \right]^2} \quad (6.19)$$

and

$$\delta_j = \text{atan} \left(\frac{\text{imag} \left(\frac{S_{j21}^+}{S_{j11}^+} \right)}{\text{real} \left(\frac{S_{j21}^+}{S_{j11}^+} \right)} \right). \quad (6.20)$$

The exciton generation rate G_j , can then be calculated, also at any position x in the multilayer, with h and c being Planck's constant and the speed of light respectively, as

$$G_j(x) = \left(\frac{\lambda}{hc} \right) Q_j(x). \quad (6.21)$$

Figure 6.8 shows the exciton generation rate through the device structure Glass/ITO 160 nm/PEDOT:PSS 30 nm/CuPc 15 nm/C₆₀ 40 nm/BCP 10 nm/Al 100 nm, as a function of position x , through the device, for all the wavelengths used in the simulation.

The exciton generation rate can then be solved, together with the steady state exciton diffusion equation

$$L_D^2 \frac{\partial^2 p}{\partial x^2} - p + \tau_j G_j = 0, \quad (6.22)$$

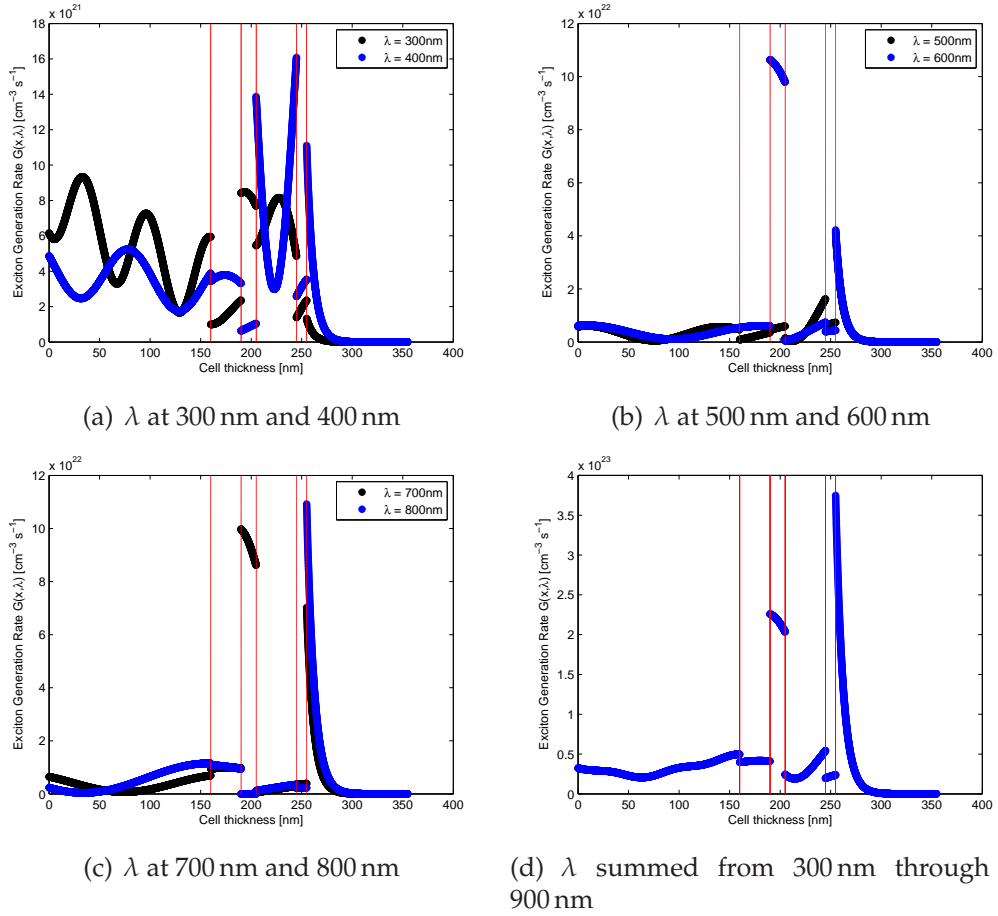


Figure 6.8: Simulated Exciton Generation Rate, as a function of wavelength and position through the whole device, for several wavelengths.

for the two active layers in Figure 6.4, i.e. the CuPc and C₆₀ layers, that contribute to photo current generation. In Equation (6.22), p is the exciton density and τ_j its lifetime.

The solution to the differential equation in (6.22), as given by [36], with N the incident photon flux (number of incident photons per unit time per unit area) and θ_1 the quantum efficiency of exciton generation, as

$$p(x) = \frac{\theta_1 \alpha T N}{D(\beta^2 - \alpha^2)} \left[A e^{-\beta x} + B e^{\beta x} + e^{-\alpha x} + C_1 e^{\alpha x} + C_2 \cos\left(\frac{4\pi n}{\lambda}(d-x) + \delta\right) \right] \quad (6.23)$$

where $\beta = 1/L_D^j = 1/\sqrt{D_j \tau_j}$, the reciprocal of the diffusion length, and D is the exciton diffusivity constant. Constants C_1 and C_2 are given by

$$C_1 = \rho^2 e^{-2\alpha d} \quad (6.24)$$

and

$$C_2 = \frac{\beta^2 - \alpha^2}{\beta^2 + \left(\frac{4\pi n}{\lambda}\right)^2} 2\rho e^{-\alpha d}, \quad (6.25)$$

while A and B are constants solved according to the boundary conditions of the model. In this case the assumption was made that all excitons either dissociate or recombine by the time they reach an interface, rendering the exciton density p , equal to zero at both ends of the layer, $x = 0$ and $x = d$. The result of these boundary conditions for solving Equation (6.23) are

$$A = \frac{e^{\beta d} - e^{-\alpha d} + C_1(e^{\beta d} - e^{\alpha d}) + C_2 \left[e^{\beta d} \cos\left(\frac{4\pi n d}{\lambda} + \delta\right) - \cos(\delta) \right]}{(e^{-\beta d} - e^{\beta d})} \quad (6.26)$$

and

$$B = -\frac{e^{-\beta d} - e^{-\alpha d} + C_1(e^{-\beta d} - e^{\alpha d}) + C_2 \left[e^{-\beta d} \cos\left(\frac{4\pi n d}{\lambda} + \delta\right) - \cos(\delta) \right]}{(e^{-\beta d} - e^{\beta d})}. \quad (6.27)$$

The short circuit exciton current density towards the donor/acceptor interface is given by

$$J_{sc} = \frac{L_D^2}{\tau_j} \left. \frac{\partial p}{\partial x} \right|_{x=x_{DA}}. \quad (6.28)$$

Thus for the two active layers, the short circuit photo current is given for layer 4, the CuPc when $x = 15$ nm, as

$$J_{photo}|_{x=d} = -q\theta J_{sc}, \quad (6.29)$$

and for layer 5, the C₆₀ when $x=0$, as

$$J_{photo}|_{x=0} = q\theta J_{sc}. \quad (6.30)$$

Substituting the distance values and the derivation of Equation (6.23), gives two equations, (6.31) and (6.32), for photo current contribution from the D/A junction.

$$J_{photo}|_{x=d} = \frac{q\theta\alpha TN}{\beta^2 - \alpha^2} \left(\beta A e^{-\beta d} - \beta B e^{\beta d} + \alpha e^{-\alpha d} - \alpha C_1 e^{\alpha d} - \frac{4\pi n}{\lambda} C_2 \sin[\delta] \right) \quad (6.31)$$

$$J_{photo}|_{x=0} = \frac{q\theta\alpha TN}{\beta^2 - \alpha^2} \left(-\beta A + \beta B - \alpha + \alpha C_1 + \frac{4\pi n}{\lambda} C_2 \sin \left[\frac{4\pi n d}{\lambda} + \delta \right] \right) \quad (6.32)$$

In Equations (6.31) and (6.32), N is given by [32] as

$$N = 10^{16} \frac{I_0 \lambda}{19.8}. \quad (6.33)$$

To compare the simulated values to the experimental values, the same variations in D/A material thicknesses were implemented in calculating the short circuit photo current density. Figure 6.9 shows the J_{photo} values for a couple of wavelengths, and the variation in active material layer thicknesses.

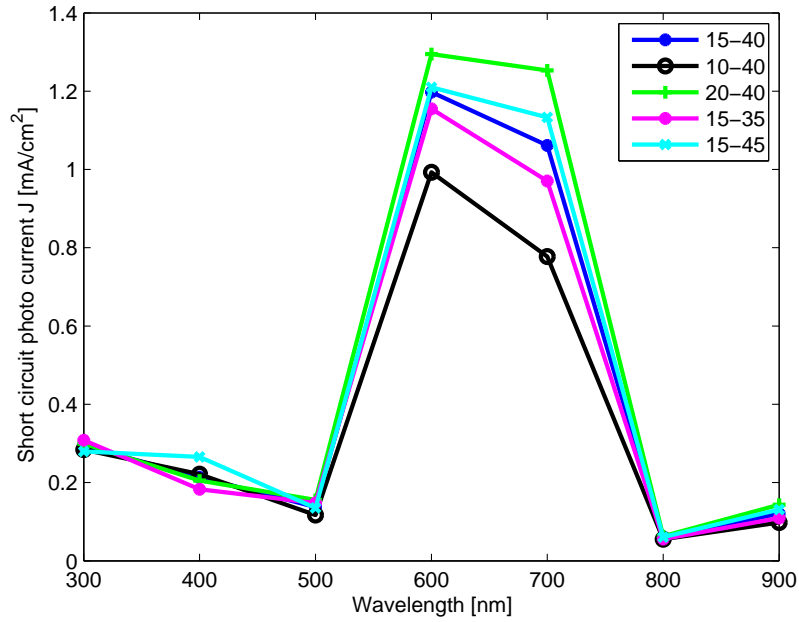


Figure 6.9: Short circuit photo current at different wavelengths, for different D/A interface thicknesses. The rest of the device structure is still the same, Glass/ITO 160 nm/PEDOT:PSS 30 nm/CuPc \times nm/C60 \times nm/BCP 10 nm/Al 100 nm, with the change in CuPc and C₆₀ thickness as indicated.

As can be seen in comparison to the absorption curve of CuPc in Figure 5.18, the current density values are a maximum between 600 nm and 700 nm, even

though the intensity for the wavelengths used were assumed to be constant. The value used for the light intensity in Equation (6.33) was assumed to be a constant 10 mW/cm^2 . This value originates from the assumption that the contribution to the total (100 mW/cm^2) light intensity between the wavelengths used (300 nm - 900 nm) is about 70 mW/cm^2 , and only 7 different wavelengths were used in the calculations.

When looking at Figure 6.9, the tendency is different than in the experimental work. Figure 6.9 shows that slightly thicker layers give higher output values. This discrepancy is attributed to the θ value used in Equations (6.31) and (6.32). In both equations, θ is the quantum efficiency of free charge generation given by

$$\theta = \theta_1 \theta_2, \quad (6.34)$$

where θ_1 and θ_2 are the quantum efficiency of exciton generation and the efficiency of the exciton dissociation at the interface respectively. In the simulations done here, θ was assumed to be unity. This is, however, not a valid assumption, since θ will differ for every variation in layer thickness, worsening for values moving away from the exciton diffusion lengths.

6.4 IV Curves

To compare the simulated values with measured experimental results, the short circuit photo generated current density, $J = 3 \text{ mA/cm}^2$ from the device simulation, with a 15/40 D/A interface, was used to generate IV curves with the model described in Section 6.2. The value for I_{ph} in the circuit is taken from the current density, as calculated from the TMM, as

$$I_{ph} = J_{ph} \cdot Area. \quad (6.35)$$

The area of the device used, was varied between 4 cm^2 and 5 cm^2 , which is approximately the area of the device as taken between the areas created by the smallest and biggest masks during thermal evaporation. The implicit equation (6.1) for the current was solved using the Newton method, as shown in Appendix C. As a lower limit, values for the series and shunt resistances were modified from [4] as

$$r_s = \frac{2.5}{Area'} \quad (6.36)$$

and

$$r_p = \frac{250}{Area}. \quad (6.37)$$

The resulting plot of the current as a function of voltage (IV), with changing area, can be seen in Figure 6.10.

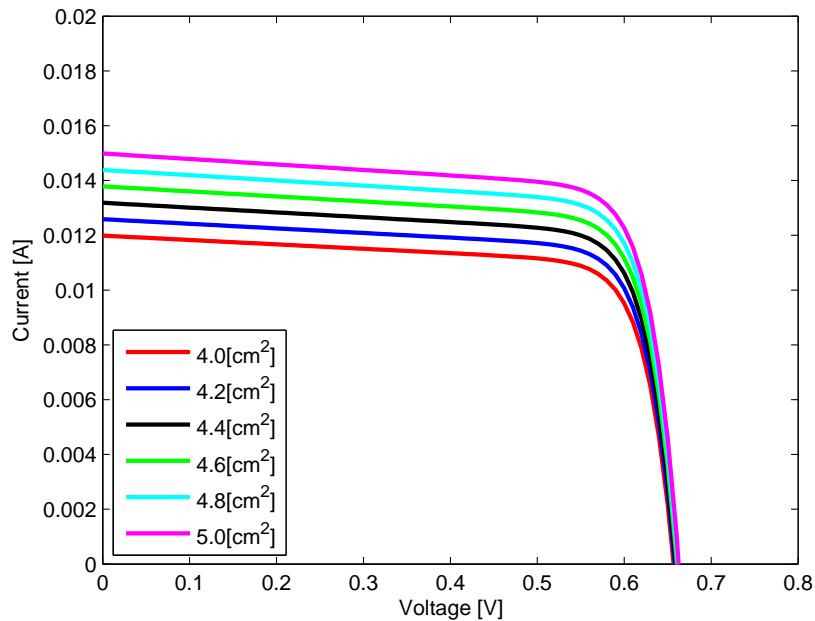


Figure 6.10: Simulated IV curve, with different cell area values. The area is varied between 4 cm^2 and 5 cm^2 , approximately the area values for the smallest and largest mask areas respectively.

As can be seen in Figure 6.10, the value of the open circuit voltage (V_{oc}) is independent from the cell area. To illustrate the effect that changes in r_s and r_p have on the slope of the graph, values measured from UCT was substituted in place of the limits used above. In Figure 6.11, r_p is kept constant, and r_s is varied through the different values for series resistance measured at UCT. While in Figure 6.12, r_s is kept constant with variation in r_p .

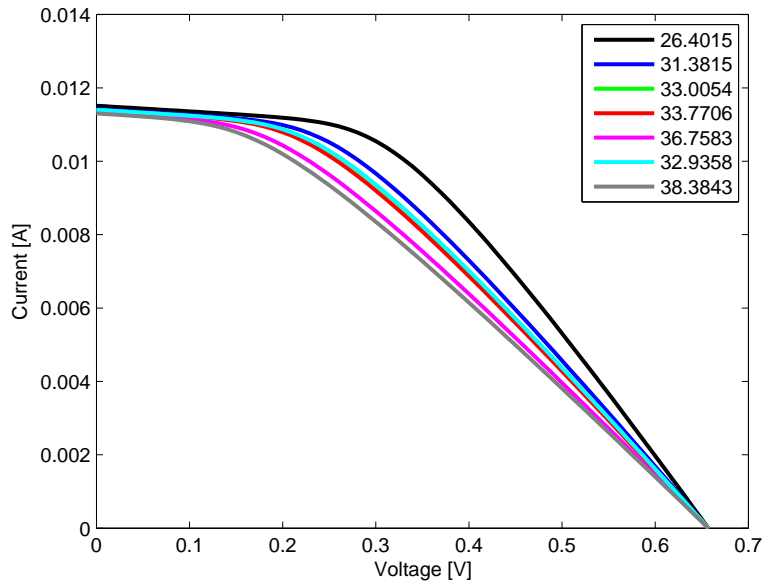


Figure 6.11: Simulated IV curve, with different series resistance values as indicated. Values used for r_s originates from values measured at UCT.

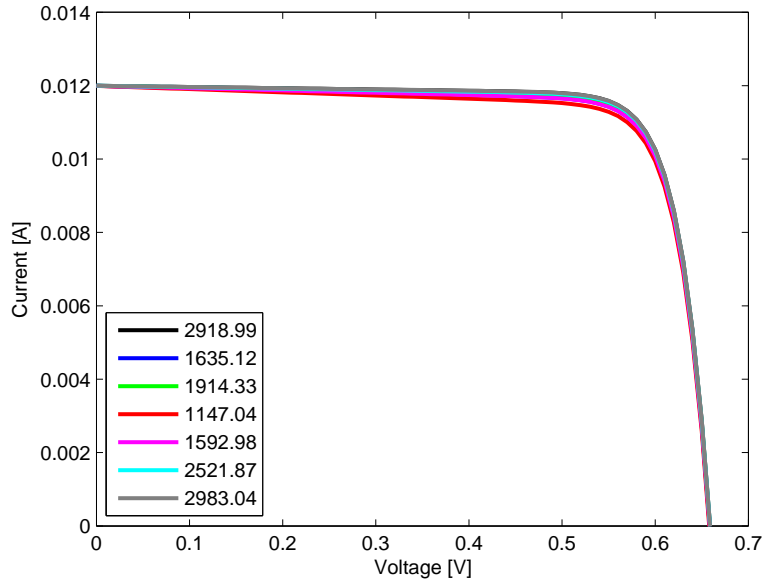


Figure 6.12: Simulated IV curve, with different shunt resistance values as indicated. Values used for r_p originates from values measured at UCT.

As can be seen in Figure 6.13, the simulated plot is bigger than the experimental result by around a factor of five. This is contributed to the assumptions made in the TMM highlighted in Section 6.3. However, the model still fits reasonably

well, as can be seen in Figure 6.14, were the values for I_{ph} , r_s and r_p used in the equivalent circuit simulation, were taken from the measured experimental results.

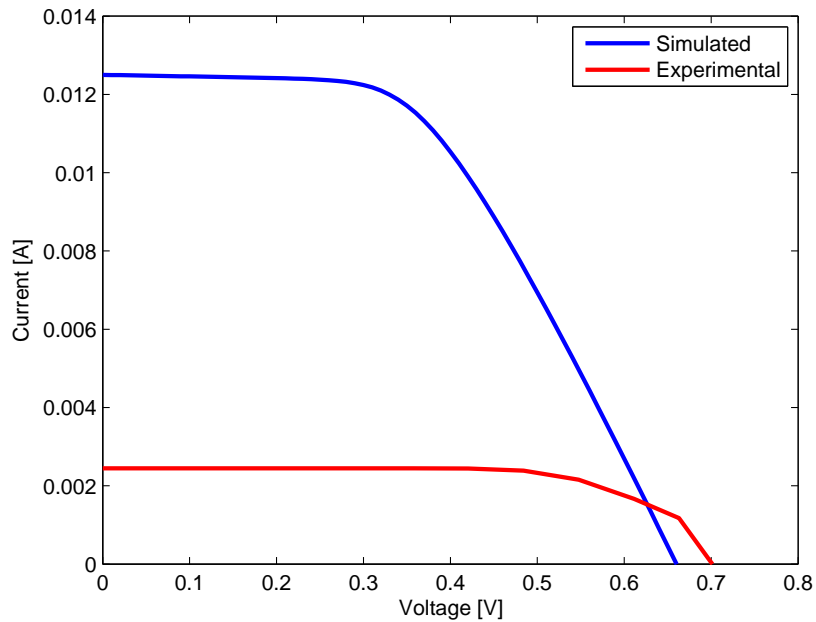


Figure 6.13: Comparison between simulated and experimental IV curve.

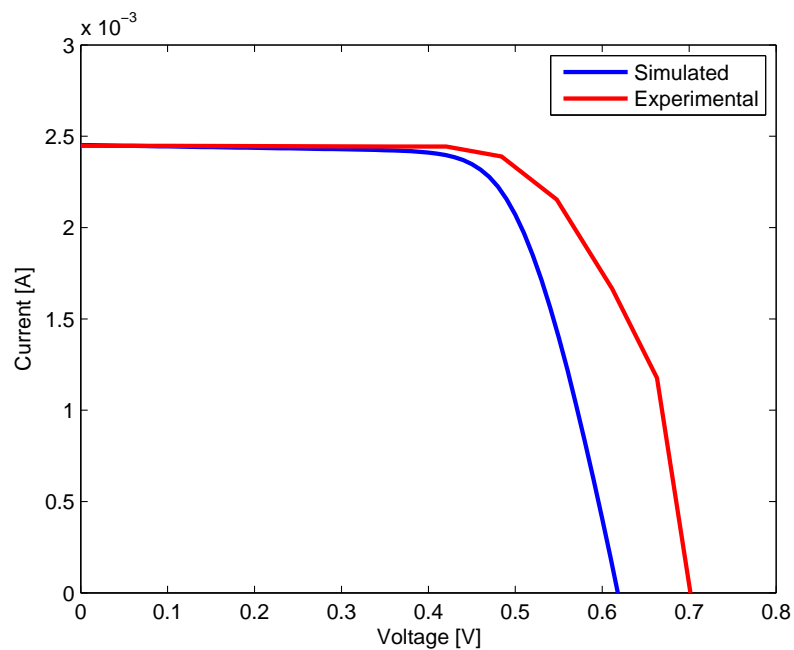


Figure 6.14: Comparison between simulated (corrected) and measured IV curve. Values for I_{ph} , r_s and r_p taken from measured experimental results.

6.5 Conclusion

The functions used to calculate the transfer matrix equations are shown in Appendix C. The functions were included as a reference for future work, as the equations were modified for some of the layers where the formulations given by [18] and [36] are not applicable for all the layers.

Chapter 7

Conclusion

This thesis has shown the design of an organic thin film photovoltaic device. All the steps needed to manufacture the device were outlined, and material thickness calibration was completed on all the materials used. Working solar cells were built, and optimal thicknesses were iteratively found for the semiconductor layers. The incident light transmitting through and reflecting off the device was estimated through calculation of the optical electric field with the TMM, as it propagated through the device. The photo generated short circuit current of the device was estimated, and an equivalent model was used to show that the behaviour of organic photovoltaic cells can be predicted.

This thesis has thus shown that thin film solar cells can be built with the equipment available to the research group. The average power conversion efficiency of the devices built and tested under 1 sun AM1.5G conditions was around 4%. This should, however, be seen as a lower limit, proving that organic photovoltaic cells with at least 4% efficiency can be built, but several possibilities can still be investigated to improve on that. Section 7.1 outlines a few recommendations for future research on the topic.

7.1 Future Recommendations

The importance of the work done here is realised when looking at the device in Chapter 3.1.4. This is the proposed future of organic photovoltaics, and its potential is shown in literature. However, there is yet to be a technique developed to realise this device, even at laboratory level. As nanotechnology is part of the research group's focus, this subject should, however, be pursued further.

Some other aspects to consider, when continuing research on this topic, include:

ITO patterning could be investigated to remove the risk of short circuits during testing. One possible example would be to remove ITO on the glass underneath where external contact will be made to the aluminium or back contact. This will result in more rugged devices.

Different materials with better absorption properties over other wavelengths could be pursued.

The Full spectrum of wavelengths should be taken into consideration when performing the TMM to calculate the photo generated current. Only a few wavelengths were considered here, for simplistic reasons, to illustrate the concept. However, all the wavelengths, with their respective complex indices of refraction should be taken into account, along with using the correct intensity profile over the spectrum to get the total intensity. (The assumption was made in this thesis that it is constant.)

The quantum efficiency of free charge generation (θ), in the simulation, should be accurately estimated. It was assumed to be unity in this work, and as a result the photo generated current estimation was too big. The actual estimation for θ should be closer to the efficiency of the cell, as [18] predicts the external quantum efficiency of the device to be $\eta_{EQE} = \eta_A \cdot \eta_{ED} \cdot \eta_D \cdot \eta_{CC}$. This efficiency reduces to the product of just the efficiency of absorption leading to exciton generation and the efficiency of exciton diffusion towards a D/A interface (the two terms θ consist of in the simulation), as the efficiency of dissociation at an interface and the collection of free charge carriers at the electrodes are normally assumed to be 100 %.

Device degradation resulting from the influence of air and moisture was not considered in this thesis.

Flexible devices were built by using a flexible substrate instead of a superstrate approach as with the ITO glass. The benefit of building from the substrate up, is that the harshest deposition (back metal electrode) is deposited first. Flexible substrates such as transparencies an polyimide was taken, covered with either aluminium or gold, before the rest of the materials were deposited as before, with the inverse of the pyramid form. Lastly, the PEDOT was spun on for the top contact. However, none of the devices built in this

manner could provide any output. The measured resistance was, however, much higher than in the other devices. Flexible solar cells should be pursued further, and other options for flexible substrates, such as FTO (FTO is more expensive than ITO, but it possesses a smoother surface roughness) on poly-propylene could be investigated.

Different exciton blocking materials could be investigated. BCP used in this project could be replaced by LiF (Lithium Fluoride). The effect of this changes was not investigated because of the toxic nature of LiF.

Equipment upgrades could be made, such as multiple sources in the thermal evaporator, automated masks and shutters etc.

Spin casting equipment could be upgraded, with greater control in ramping up the initial velocity. This is a critical area as it was shown that the PEDOT film thickness, manufactured by spin casting, was difficult to control.

Dust control could be improved by renovating existing laminar flow chambers.

Appendices

Appendix A

Shadow Masks Used in Thermal Evaporation

Due to the fact that samples are placed upside down in the thermal evaporator, masks were made to hold the samples in place above the plume, and serve as shadow masks. All the masks were designed to fit around a square stainless steel block, 40 mm by 40 mm, which was used as a sample heater. This meant that the sample heater could stay fixed in the thermal evaporator, saving time and effort in connecting the wires into the vacuum chamber each time it was needed. It also ensured that a temperature could be applied the sample for the deposition of any layer.

The masks were designed in Autodesk's Inventor package. A sheet metal part was created and unfolded to get the dimensioning for the fold line, to ensure that the masks fit tightly around the sample heater. Two 0.5 mm stitching lines were put on the fold lines to ensure the masks bent at the correct width, ensuring a 40 mm gap between flanges. Slots were cut in the edges outside the fold lines, such that the masks could be slid over the sample heater and screwed on, as illustrated in Figure A.1.

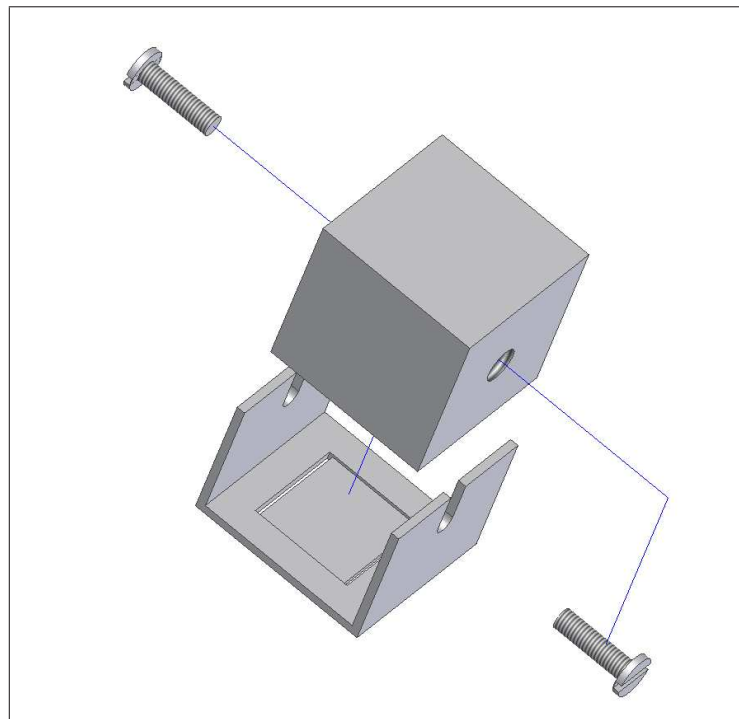


Figure A.1: Representation of how the masks, one in this case, are bent to fit around the sample heater.

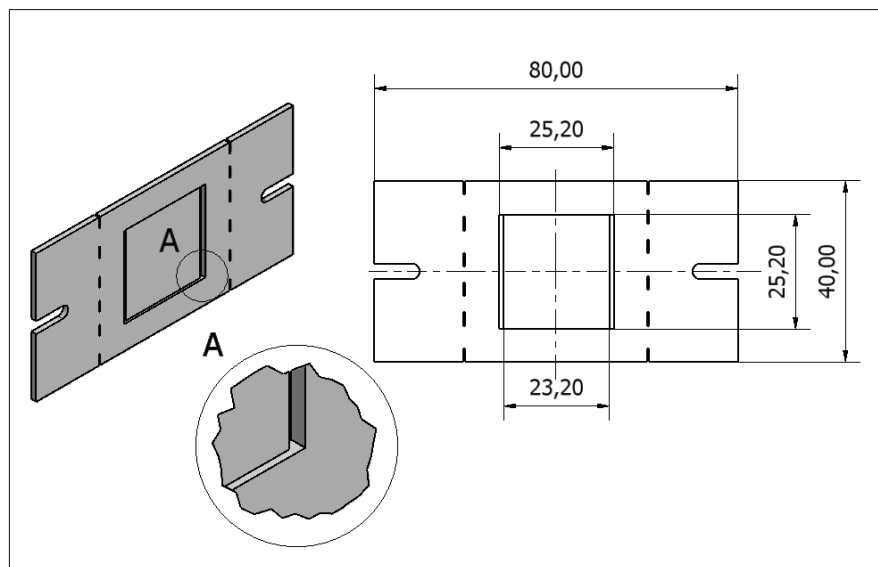


Figure A.2: Mask 1. Used to deposit two $1\text{ mm} \times 25\text{ mm}$ strips of silver on the edges of the ITO glass.

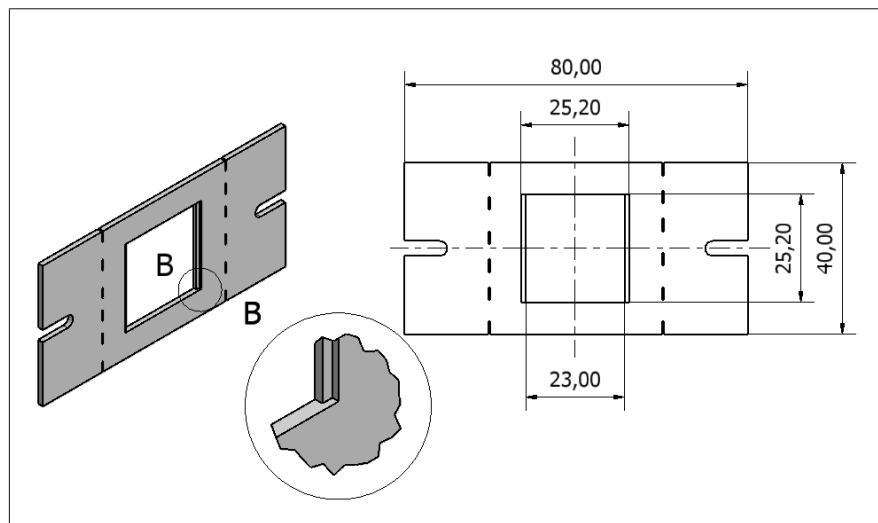


Figure A.3: Mask 2. Used to deposit CuPc between the silver strips made with Mask 1. Dimensioned that a 23 mm × 25 mm area of CuPc could be deposited

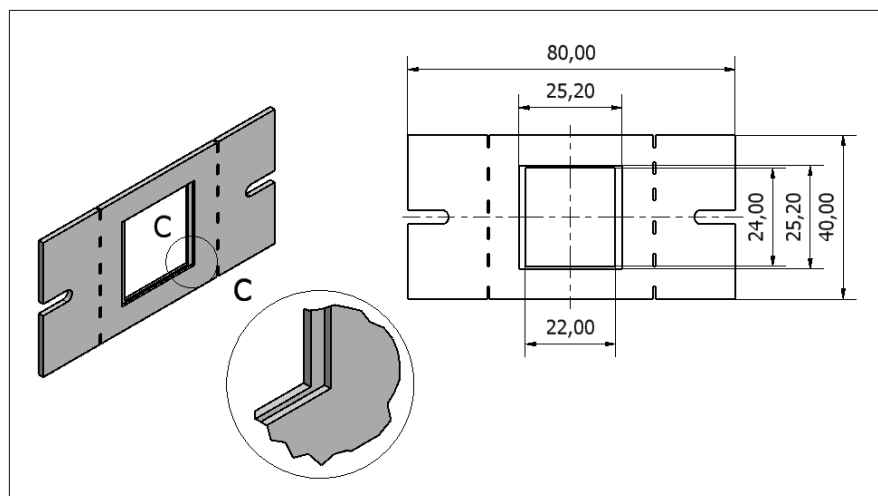


Figure A.4: Mask 3. Used to deposit C₆₀ on top of the CuPc. Dimensioned that a 22 mm × 24 mm area of C₆₀ could be deposited to ensure that the C₆₀ did not overlap the CuPc layer.

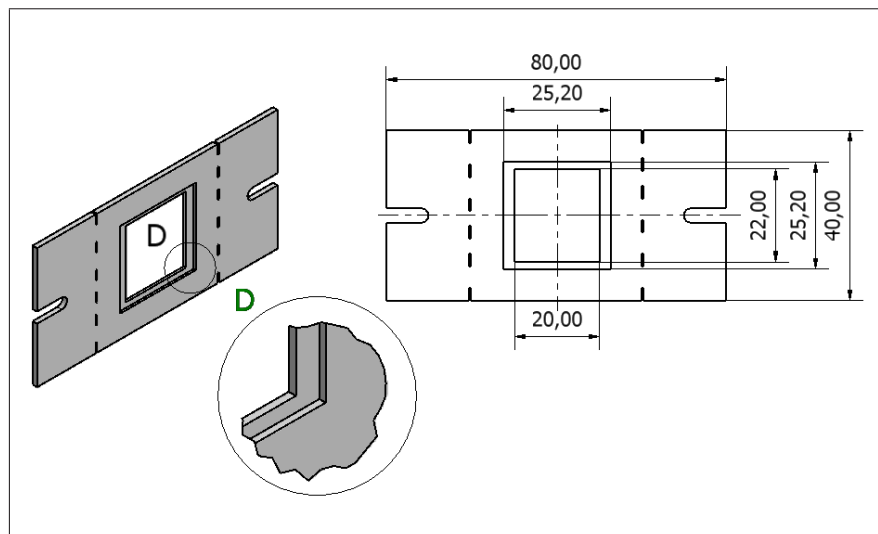


Figure A.5: Mask 4. Used to deposit the aluminium layer. Dimensioned that a 20 mm \times 22 mm area of aluminium could be deposited. These values are small enough to ensure no overlapping between the aluminium and C_{60} , as well as making provision for an exciton blocking layer.

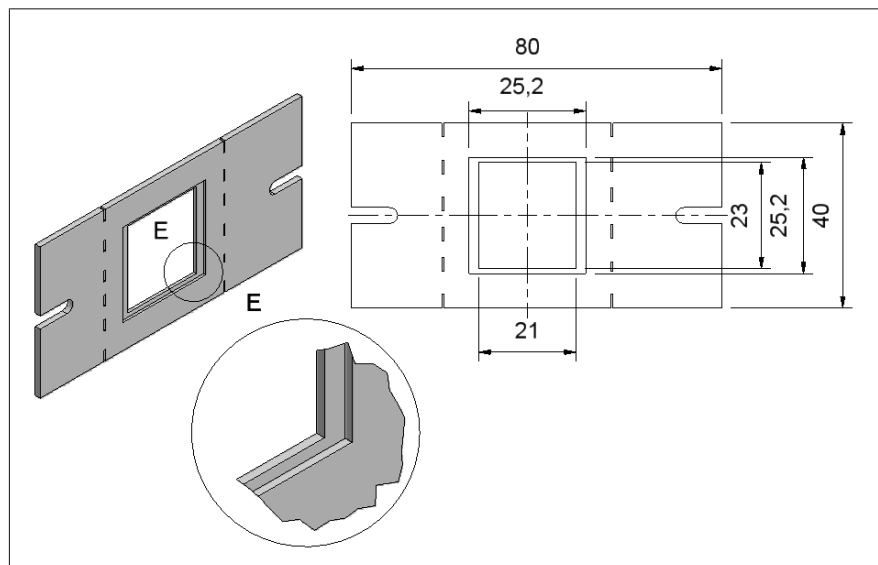


Figure A.6: Mask 5. Used to deposit BCP. Dimensioned to form a 21 mm \times 23 mm area of BCP. This ensures that the BCP layer fits between the C_{60} and aluminium in the pyramid style.

Appendix B

Complex indices of refraction

Table B.1: Complex indices of refraction for PEDOT:PSS at different wavelengths taken from [6]

λ (nm)	Optical indices (n)	Extinction coefficients (k)
300	1.75	0.1
400	1.66	0.05
500	1.59	0.04
600	1.5	0.06
700	1.49	0.08
800	1.5	0.07
900	1.49	0.06

Table B.2: Complex indices of refraction for aluminium at different wavelengths taken from [7]

λ (nm)	Optical indices (n)	Extinction coefficients (k)
300	0.28	3.6
400	0.5	4.8
500	0.8	6.1
600	1.25	7.2
700	1.85	8.1
800	2.68	8.49
900	2.75	8.7

Table B.3: Complex indices of refraction for ITO at different wavelengths taken from [8]

λ (nm)	Optical indices (n)	Extinction coefficients (k)
300	2.4	0.15
400	2.05	0.07
500	1.9	0.05
600	1.8	0.05
700	1.75	0.05
800	1.6	0.07
900	1.55	0.075

Table B.4: Complex indices of refraction for BCP at different wavelengths taken from [9]

λ (nm)	Optical indices (n)	Extinction coefficients (k)
300	1.775	0.25
400	1.825	0.06
500	1.74	0.04
600	1.7	0.03
700	1.67	0.02
800	1.66	0.01
900	1.64	0

Table B.5: Complex indices of refraction for CuPc at different wavelengths taken from [10]

λ (nm)	Optical indices (n)	Extinction coefficients (k)
300	1.65	0.35
400	2.0	0.02
500	1.61	0.05
600	1.72	0.92
700	2.3	0.53
800	2.24	0
900	2.09	0.04

Table B.6: Complex indices of refraction for PEDOT:PSS at different wavelengths taken from [10]

λ (nm)	Optical indices (n)	Extinction coefficients (k)
300	2.13	0.62
400	2.19	0.47
500	2.3	0.14
600	2.11	0.07
700	2.05	0.02
800	2.02	0.02
900	2.0	0.02

Appendix C

TMM

Listing C.1: Functions for calculating the transfer matrix and optical electric field.

```
%% Rev- Journal of applied physics vol 93, number 7 2003. pg 3693
% E0 % % % % % % m % m+1
% j=1 % j=2 % j=3 % j=4 % j=5 % j=6 % j=7 %
% % % % % % % %
% glass % ITO % PSS: % CuPc % C60 % BCP % Al % air
% % % PEDOT % % % %
% % % % % % % %

% This is the main function of the simulation to characterise an organic
% solar cell.
clear all;
close all;
clc;
global layer_thickness; % physical thickness of each material layer
global lambda; % wavelength at which simulation is being performed
global n; % real componenet of complex refraction of a specific layer at the
% given wavelength
global k; % complex componenet of complex refraction of a specific layer at
% the given wavelength
global L_D; % exciton diffusion length
global layer; % counter through the layers of the structure
global c; % speed of light
global tau; % lifetime of the exciton
global h;
global Isetup;
global Lsetup;
global Splussetup;
global Sminsetup;
global rtwosetup;
global tplussetup;
global tminsetup;

I0 = 100; % mW/cm^2 (100e-5 for G to be in S^-1cm^-3)
e_0 = 8.85418782e-12;
E0 = 86.8;
Jphoto = zeros(7,1);
```

```

layer_thickness = [0.7e-3 1600e-10 300e-10 150e-10 400e-10 100e-10 1000e-10]; % [m]
Gsum = zeros(1, 8000);
q = 1.60218e-19;
c = 299792458;
L_D = [1 1 1 150e-10 400e-10 1 1 1]; % [m]
tau = [1 1 1 1e-8 1e-6 1 1 1];
h = 6.626068e-34;
einde = 0;
jl = 1;

for lambda = 300e-9:100e-9:900e-9
    if lambda == 300e-9
        n = [1.42 2.4 1.75 1.65 2.13 1.775 0.28 1];
        k = [0 0.15 0.1 0.35 0.62 0.25 3.6 0];
        colour = 'k*';
    elseif lambda == 400e-9
        n = [1.42 2.05 1.66 2.0 2.19 1.825 0.5 1];
        k = [0 0.07 0.05 0.02 0.47 0.06 4.8 0];
        colour = 'blue*';
    elseif lambda == 500e-9
        n = [1.42 1.9 1.59 1.61 2.3 1.74 0.8 1];
        k = [0 0.05 0.04 0.05 0.14 0.04 6.1 0];
        colour = 'k*';
    elseif lambda == 600e-9
        n = [1.42 1.8 1.5 1.72 2.11 1.7 1.25 1];
        k = [0 0.05 0.06 0.92 0.07 0.03 7.2 0];
        colour = 'blue*';
    elseif lambda == 700e-9
        n = [1.42 1.75 1.49 2.3 2.05 1.67 1.85 1];
        k = [0 0.05 0.08 0.53 0.02 0.02 8.1 0];
        colour = 'k*';
    elseif lambda == 800e-9
        n = [1.42 1.6 1.5 2.24 2.02 1.66 2.68 1];
        k = [0 0.07 0.07 0.0 0.02 0.01 8.49 0];
        colour = 'blue*';
    else
        n = [1.42 1.55 1.49 2.09 2.0 1.64 2.75 1];
        k = [0 0.075 0.06 0.04 0.02 0 8.7 0];
        colour = 'magenta*';
    end
end
%Ivalues
Isetup = zeros(14,2);
for layer = 1:1:7
    t = (2*(n(layer) + i*k(layer)))/((n(layer) + i*k(layer)) + (n(layer+1)
        + i*k(layer+1)));
    r = ((n(layer) + i*k(layer)) - (n(layer+1) + i*k(layer+1)))/((n(layer)
        + i*k(layer)) + (n(layer+1) + i*k(layer+1)));
    I = [1/t r/t; r/t 1/t];
    xpos = layer + layer - 1 ;

    for x = 0:1:1
        for y = 1:1:2
            Isetup((xpos+x),y) = I((x+1),y);
        end
    end
end

```

```

        end
    end
% Zvalue-----
    zvalue = zeros(7,1);
    for layer=1:1:7
        zvalue(layer) = (2*pi/lambda)*(n(layer) + i*(k(layer)));
    end
% Lvalue-----
    Lsetup = zeros(14,2);
    for layer=1:1:7
        L = [exp(-i*zvalue(layer)*layer_thickness(layer)) 0;
            0 exp(i*zvalue(layer)*layer_thickness(layer))];
        xpos = layer + layer -1 ;
        ypos = 1;
        for x = 0:1:1
            for y = 1:1:2
                Lsetup((xpos+x),y) = L((x+1),y);
            end
        end
    end
% Splus S'-----
    Splussetup = zeros(14,2);
    for layer = 2:1:7
        S2 = [1 0; 0 1];
        for tel=layer:6
            S2 = S2*Ivalue(tel)*Lvalue(tel+1);
        end
        if(layer == 7)
            S2 = Ivalue(7);
        end
        xpos = layer + layer -1;
        for x = 0:1:1
            for y = 1:1:2
                Splussetup((xpos+x),y) = S2((x+1),y);
            end
        end
    end
% Smin S'-----
    Sminsetup = zeros(14,2);
    for layer = 2:1:7
        S2 = Ivalue(1);
        for tel=3:layer
            S2 = S2*Lvalue(tel-1)*Ivalue(tel-1);
        end
        xpos = layer + layer -1;
        for x = 0:1:1
            for y = 1:1:2
                Sminsetup((xpos+x),y) = S2((x+1),y);
            end
        end
    end
% rtwo-----
    rtwosetup = zeros(7,1);
    for layer = 2:1:7

```

```

        r2 = Splusvalue(layer,2,1)/Splusvalue(layer,1,1);
        rtwosetup(layer) = r2;
    end
% tplus-----
    tplussetup = zeros(7,1);
    for layer = 2:1:7
        t2 = (1/Sminvalue(layer,1,1))/(1 + ((Sminvalue(layer,1,2)*Splusvalue(layer,2,1))/
            (Sminvalue(layer,1,1)*Splusvalue(layer,1,1)))*exp(i*2*zvalue(layer)*
            layer_thickness(layer)));
        tplussetup(layer) = t2;
    end
% tmin-----
    tminsetup = zeros(7,1);
    for layer = 2:1:7
        t2 = tplusvalue(layer)*(Splusvalue(layer,2,1)/Splusvalue(layer,1,1))*
            exp(i*2*zvalue(layer)*layer_thickness(layer));
        tminsetup(layer) = t2;
    end
% alpha-----
    alpha = zeros(7,1);
    for layer = 2:1:7
        alpha(layer) = 4*pi*k(layer)/lambda;
    end
% delta-----
    delta = zeros(7,1);
    for layer = 2:1:7
        delta(layer) = atan(imag(rtwovalue(layer))/real(rtwovalue(layer)));
    end
% rho-----
    rho = zeros(7,1);
    for layer = 2:1:7
        rho(layer) = sqrt((imag(rtwovalue(layer))^2 + (real(rtwovalue(layer)))^2));
    end
% T-----
    T = zeros(7,1);
    for layer = 2:1:7
        T(layer) = (n(layer)/n(1))*(abs(tplusvalue(layer)))^2;
    end
% Big for loop-----
    fake_d = zeros(7,1);
    fake_d(1) = 0.0;
    for count=2:1:7
        fake_d(count) = fake_d(count-1) + layer_thickness(count);
        einde = einde + layer_thickness(count);
    end
    m=1;
    temp=0;
    dt = 0.5e-10;
    Efield = zeros(ceil(einde/dt),1);
    for layer=2:1:7
        x = 0:dt:layer_thickness(layer);
        loopeinde = layer_thickness(layer)/dt;
        E = zeros(ceil(loopeinde),1);
        for y = 1:1:loopeinde

```



```

E(y) = ((Splusvalue(layer, 1, 1)*exp(-i*zvalue(layer)*(layer_thickness(layer)
- x(y))) + Splusvalue(layer, 2,1)*exp(i*zvalue(layer)*
(layer_thickness(layer) - x(y))))/(Sminvalue(layer,1,1)*
Splusvalue(layer,1,1)*exp(-i*zvalue(layer)*layer_thickness(layer))
+ Sminvalue(layer, 1,2)*Splusvalue(layer, 2, 1)*
exp(i*zvalue(layer)*layer_thickness(layer))));
Efield(m) = E(y);
Q(y) = alpha(layer)*T(layer)*I0*((exp(-alpha(layer)*x(y))) + (rho(layer)^2*
exp(-alpha(layer)*(2*layer_thickness(layer)-x(y)))) + (2*rho(layer)*
exp(-alpha(layer)*layer_thickness(layer))*cos(((4*pi*n(layer)*
(layer_thickness(layer)- x(y))/lambda) + (delta(layer))))));
Qfield(m) = Q(y);
if ((layer ==4) || (layer == 5))
    Gfield(m) = (lambda/(h*c))*Qfield(m);
end
m = m+1;
end
end
temp = size(Gfield(:));
Gsum(1,1:temp(1)) = Gsum(1,1:temp(1)) + Gfield(1,1:temp(1));
x = 0:dt:einde;
for layer =4:1:5
    alpha = (4*pi*k(layer))/lambda;
    beta = 1/L_D(layer);
    d = layer_thickness(layer);
    eff = n(layer);
    theta = 1;
    N = (1e16*(I0*10*lambda*1e6)/19.8); % converts Jphoto to mA/cm^2
    D = (L_D(layer))^2/tau(layer);

    r = (Splusvalue(layer, 2, 1))/(Splusvalue(layer, 1, 1));
    delta = atan(imag(r)/real(r));
    rho = sqrt((imag(r))^2 + (real(r))^2);

    T = ((n(layer))/(n(1)))*(abs(tplusvalue(layer)))^2;

    C1 = rho^2*exp(-2*alpha*d);
    C2 = ((beta^2 - alpha^2)/(beta^2 + (4*pi*eff/lambda)^2))*2*rho*exp(-1*alpha*d);

    A = ((exp(beta*d) - exp(-1*alpha*d)) + C1*(exp(beta*d) - exp(alpha*d))
+ C2*(exp(beta*d)*cos((4*pi*eff*d/lambda) + delta) - cos(delta)))/
(exp(-1*beta*d) - exp(beta*d));

    B = -1*(((exp(-1*beta*d) - exp(-1*alpha*d)) + C1*(exp(-1*beta*d) - exp(alpha*d))
+ C2*(exp(-1*beta*d)*cos((4*pi*eff*d)/lambda) + delta) - cos(delta)))/
(exp(-1*beta*d) - exp(beta*d));

    if layer ==5
        Jphoto_0 = ((q*theta*alpha*T*N)/(beta^2 - alpha^2))*((-1*beta*A) + (beta*B)
- (alpha) + (alpha*C1) + (((4*pi*eff)/lambda)*
C2*sin(((4*pi*eff*d)/lambda) + (delta))));
        Jphoto(jl) = Jphoto_0 + Jphoto(jl);
    elseif layer ==4
        Jphoto_d = ((q*theta*alpha*T*N)/(beta^2 - alpha^2))*((beta*A*exp(-beta*d))

```

```

        - (beta*B*exp(beta*d)) + (alpha*exp(-alpha*d))
        - (alpha*C1*exp(alpha*d)) - (((4*pi*eff)/lambda)*C2*sin(delta));
    Jphoto(jl) = Jphoto_d + Jphoto(jl);
    end
end
jl = jl + 1;
end
%%-----
function f = Ivalue(layer)
global Isetup;
f = zeros(2,2);
temp = zeros(2,2);
posx = layer + layer - 1;
for x = 0:1:1
    for y = 1:1:2
        temp ((x+1),y) = Isetup((posx+x),y);
    end
end
f = temp;
%%-----
function f = Lvalue(layer)
global Lsetup;
f = zeros(2,2);
temp = zeros(2,2);
posx = layer + layer - 1;
for x = 0:1:1
    for y = 1:1:2
        temp ((x+1),y) = Lsetup((posx+x),y);
    end
end
f = temp;
%%-----
function f = Splusvalue(layer , a , b)
global Splussetup;
temp = zeros(2,2);
posx = layer + layer - 1;
for x = 0:1:1
    for y = 1:1:2
        temp ((x+1),y) = Splussetup((posx+x),y);
    end
end
f = temp(a , b);
%%-----
function f = Sminvalue(layer , a , b)
global Sminsetup;
temp = zeros(2,2);
posx = layer + layer - 1;
for x = 0:1:1
    for y = 1:1:2
        temp ((x+1),y) = Sminsetup((posx+x),y);
    end
end
f = temp(a , b);
%%-----

```

```

function f = rtwovalue(layer)
global rtwosetup;
f = rtwosetup(layer);
%%-----
function f = tplusvalue(layer)
global tplussetup;
f = tplussetup(layer);
%%-----
function f = tminvalue(layer)
global tminsetup;
f = tminsetup(layer);

```

Listing C.2: Function for solving the implicit equation for current in the equivalent circuit model.

```

n = 1;
for V = -0.8:0.01:0.8 % in V

    % guess for In in A
    In = 1e-3;
    condition = 1;
    while (condition ~= 0)
        F = In - Iph + Is*(exp((q*(V + rs*In))/(k*T)) - 1) + ((V + rs*In)/rp);

        Fderiv = rs/rp + 1 + (Is*q*rs*exp((q*(V + rs*In))/(k*T)))/(k*T);

        Inew = In - F/Fderiv;
        error = abs(Inew - In);
        if (error < 1e-10)
            condition = 0;
        else
            In = Inew;
        end
    end
    Vplot(n) = V;
    Iplot(n) = Inew;
    n = n+1;
end

```

References

- [1] Neamen, D.A.: *Microelectronics Circuit Analysis and Design*. 3rd edn. McGraw Hill, 2007.
- [2] Shich-Chang Suen *et al*: Low-temperature self-assembly of copper phthalocyanine nanofibers. *Organic Electronics*, vol. 7, pp. 428–434, 2006.
- [3] Mazhari, B.: An improved solar cell model for organic solar cells. *Solar Energy Materials & Solar Cells*, vol. 90, pp. 1021–1033, 2006.
- [4] Moliton, A. and Jean-Michel Nunzi: How to model the behaviour of organic photovoltaic cells. *Polymer International*, vol. 55, pp. 583–600, 2006.
- [5] Sam-Shajing Sun: *Advances in Solar Energy: An annual Review of research and Development*, vol. 17. American Solar Energy Society, 2007. Chapter 3.
- [6] L.A.A Pettersson *et al*: Anisotropic optical properties of doped poly(3,4-ethylenedioxythiophene). *Synthetic Metals*, vol. 101, pp. 198–199, 1999.
- [7] S. Van Gils *et al*: Colour properties of barrier anodic oxide films on aluminium and titanium studied with total reflectance and spectroscopic ellipsometry. *Surface & Coatings Technology*, vol. 185, pp. 303–310, 2004.
- [8] R.A Synowicki: Spectroscopic ellipsometry characterization of indium tin oxide film microstructure and optical constants. *Thin Solid Films*, vol. 313, pp. 394–397, 1998.
- [9] Z.T. Liu *et al*: The characterization of the optical functions of bcp and cbp thin films by spectroscopic ellipsometry. *Synthetic Metals*, vol. 150, pp. 159–163, 2005.
- [10] Florent Monestier *et al*: Optical modeling of organic solar cells based on cupc and c₆₀. *Applied Optics*, vol. 47, pp. 251–256, 2008.
- [11] Ben Rogers *et al*: *Nanotechnology Understanding Small Systems*. CRC Press, 2008.
- [12] Messenger, R. and Ventre, J.: *Photovoltaic Systems Engineering*. CRC Press, 2000.
- [13] Alex C. Mayer *et al*: Polymer-based solar cells. *Materials Today*, vol. 10, pp. 28–33, 2007.

- [14] Vargas, W.E. and Niklasson, G.A.: Optical properties of nano-structured dye-sensitized solar cells. *Solar Energy Materials & Solar Cells*, vol. 69, pp. 147–163, 2001.
- [15] Chiumg-Wei Lin et al: Effect of in-grain porous silicon structure on photovoltaic device. *Journal of Physics and Chemistry of Solids*, vol. 69, pp. 641–644, 2008.
- [16] Imahori, H.: Creation of Fullerene-Based Artificial Photosynthetic Systems. *The Chemical Society of Japan*, vol. 80, pp. 621–636, 2007.
- [17] Zhou, J.: *Handbook of Nanophase and Nanostructured Materials*, vol. 1. Kluwer Academic/Plenum Publishers, 2003.
- [18] Peter Peumans et al: Small molecular weight organic thin-film photodetectors and solar cells. *Journal of Applied Physics*, vol. 93, pp. 3693–3723, 2003.
- [19] Chih-ta Wang and Shi-Chern Yen: Theoretical analysis of film uniformity in spinning processes. *Chemical Engineering Science*, vol. 50, pp. 989–999, 1995.
- [20] Heavens, O.: *Thin Film Physics*. Science Paperbacks, 1970.
- [21] Lyshevski, S.E.: *MEMS and NEMS Systems, Devices and Structures*. CRC PRESS, 2002.
- [22] Darling, R.: Photolithography. EE-527: MicroFabrication Course notes.
- [23] Sung Woo Hur et al: Organic photovoltaic effects using CuPc and C₆₀ depending on layer thickness. *Synthetic Metals*, vol. 154, pp. 49–52, 2005.
- [24] Copper Phthalocyanine CAS N^o: 147-14-8.
- [25] Dresselhaus, M.S., Ekluna, P.C. and Dresselhaus, G.: *Carbon Materials for Advanced Technologies*. Elsevier, 1999.
- [26] Yagafarov, O.F., Gromnitskaya, E.L., Lyapin, A.G., Brazhkin, V.V. and Kondrin, M.V.: Ultrasonic study of monomeric fullerite C₆₀ under pressure. *Journal of Physics: Conference Series*, vol. 121, 2008.
- [27] Kanari Moriyasu et al: Nanoindentation test for evaluating intermolecular elastic and plastic characteristics of copper phthalocyanine thin films. *Japanese Journal of Applied Physics*, vol. 44, pp. 8249–8255, 2005.
- [28] V.P. Singh et al: Characterization of high-photovoltage cupc-based solar cell structures. *Solar Energy Materials & Solar Cells*, vol. 90, pp. 798–812, 2006.
- [29] Jiangeng Xue et al: 4.2 % efficient organic photovoltaic cells with low series resistances. *Applied Physics Letters*, vol. 84, pp. 3013–3015, 2004.

- [30] Kuan-Cheng Chiu *et al*: Effects of source and substrate temperatures on the properties of ITO/CuPc/C₆₀ heterostructure prepared by physical vapor deposition. *Journal of Crystal Growth*, vol. 310, pp. 1734–1738, 2008.
- [31] Petritsch, K.: *Organic Solar Cell Architectures*. Ph.D. thesis, University of Graz Austria, 2000.
- [32] Castañer, L. and Silvestre, S.: *Modelling Photovoltaic Systems Using PSpice*. Wiley, 2002.
- [33] Markvart, T. (ed.): *Solar Electricity*. 2nd edn. Wiley, 2000.
- [34] Farag, A.A.M.: Optical absorption studies of copper phthalocyanine thin films. *Optics & Laser Technology*, vol. 39, pp. 728–732, 2007.
- [35] http://www.silvaco.com/products/vwf/atlas/organicsolar/organicsolar_br.htm:
.
- [36] Leif A. A. Pettersson *et al*: Modeling photocurrent action spectra of photovoltaic devices based on organic thin films. *Journal of Applied Physics*, vol. 86, pp. 487–496, 1999.